Progress in Oceanography 217 (2023) 103077

Contents lists available at ScienceDirect

Progress in Oceanography

journal homepage: www.elsevier.com/locate/pocean

Analysis of internal soliton signals and their eastward propagation in the Alboran Sea: exploring the effect of subinertial forcing and fortnightly variability

Marina Bolado-Penagos [a,*], Iria Sala [b,c], Juan Jesús Gomiz-Pascual [a], Carlos J. González [d], Alfredo Izquierdo [a], Óscar Álvarez [a], Águeda Vázquez [a], Miguel Bruno [a], Hans van Haren [e]

[a] Department of Applied Physics, Faculty of Marine and Environmental Sciences, Marine Research Institute (INMAR), International Campus of Excellence of the Sea (CEI·MAR), University of Cadiz, Puerto Real, 11510 Cadiz, Spain
[b] Department of Biology, Faculty of Marine and Environmental Sciences, Marine Research Institute (INMAR), International Campus of Excellence of the Sea (CEI·MAR), University of Cadiz, Puerto Real, 11510 Cadiz, Spain
[c] Department of Mathematics and Statistics, University of Strathclyde, G1 1XH Glasgow, United Kingdom
[d] Marine Hydrographic Institute (IHM), Spanish Navy, Division of Naval Support and Oceanography, Plaza San Severiano 3, 11007 Cadiz, Spain
[e] Royal Netherlands Institute for Sea Research (NIOZ), P.O. Box 59, 1790 AB Den Burg, The Netherlands

ARTICLE INFO

Keywords:
Internal solitons
Strait of Gibraltar
Alboran Sea
Upwelling
Atmospheric forcing

ABSTRACT

Internal waves are commonly observed in oceans and lakes where high stratification exists. In the present study in the Strait of Gibraltar, we analyse internal soliton signals recorded in different locations in their eastward propagation from their release point (Camarinal Sill) to the continental slope of the northwestern Alboran Sea. Moreover, the effect of subinertial forcing on the release of solitons is also explored. The internal soliton activity was assessed from different approaches: (i) in-situ data (i.e., current and temperature measurements or High-Frequency Radar), (ii) numerical modelling, and (iii) an analytical approach. The arrival of solitons over the continental slope of the north-western Alboran Sea showed fortnightly variability in both number (occurrence) and amplitude during spring tides when compared with during neap tides. The observed arrival times of the solitons oscillated between 14 (spring tides) and 20 h (neap tides). Nevertheless, to provide a comprehensive explanation for the fluctuations in travel times, it is necessary to consider the subinertial variability driven by atmospheric forcing, which impacts both the flow in the Strait of Gibraltar and the mesoscale patterns in the Alboran Sea (e.g., the Coastal Cyclonic Gyre).

1. Introduction

Inflowing Atlantic water meets outflowing Mediterranean water in the Strait of Gibraltar, where a baroclinic exchange has been widely studied (e.g., Criado-Aldeanueva et al., 2012). The less-dense upper Atlantic water flows eastwards into the Alboran Sea as a meandering jet, known as the Atlantic jet, which varies seasonally (Macías et al., 2016) and drives the main circulation pattern within the upper 100–150 m of the water column in the Alboran Sea (Oguz et al., 2017). The denser and saltier Mediterranean water, a mixture of Mediterranean water masses (e.g., Millot, 2009), flows westward at greater depths towards the Atlantic Ocean.

Therefore, the circulation through the Strait of Gibraltar is commonly simplified as a two-layer inverse-estuarine exchange (Armi and Farmer, 1988), and the interaction between both water masses constitute the Atlantic-Mediterranean Interface (AMI), which is saltier, warmer, and shallower on the eastern side of the Strait than on the western side (Bray et al., 1995).

The irregular bottom topography of the Strait of Gibraltar dominates the main hydrodynamic processes there. The Atlantic inflow is hydraulically controlled by the narrowest section of the Strait, the Tarifa Narrows (TN in Fig. 1a), where a thicker AMI is depicted (García-Lafuente et al., 2002a). The Mediterranean water outflow is controlled by the main sills of the Strait (Armi and Farmer, 1985; García-Lafuente et al., 2002a; Sánchez-Román et al., 2009), located west from TN: Espartel (~360 m) and Camarinal Sills (~290 m; CS) (see Fig. 1a).

CS has been the focus of several studies since the interaction of the barotropic tidal flow with the bathymetric feature generates large

* Corresponding author.
E-mail address: marina.bolado@uca.es (M. Bolado-Penagos).

https://doi.org/10.1016/j.pocean.2023.103077
Received 13 March 2023; Received in revised form 9 May 2023; Accepted 17 June 2023
Available online 22 June 2023

amplitude internal waves over the Sill (e.g., Brandt et al., 1996; Izquierdo et al., 2001) during most tidal cycles. As described by Vázquez et al. (2008), these so-called A-Waves (Watson and Robinson, 1990) are generated when critical flow conditions are reached over CS during the westward phase of the barotropic tidal current, which is when the maximum westward barotropic M_2 current reaches speeds of ~ 1 m s^{-1}. These conditions lead to the formation of an internal bore on the lee side of the Sill.

Using a two-layer approach, such hydraulic conditions are frequently characterized, through the internal Froude number (G^2):

$$G^2 = \frac{U_1^2}{g' h_1} + \frac{U_2^2}{g' h_2} \quad (1)$$

where $g' = g\,(\rho_2\text{-}\rho_1)\,/\,\rho_2$ is the reduced gravity; U_i, ρ_i, and h_i are the mean velocity, mean density, and thickness for each layer ($i = 1, 2$ for the upper and lower layers, respectively). Internal waves remain trapped over the Sill while critical ($G^2 = 1$) or supercritical ($G^2 > 1$) Froude number conditions prevail, during the westward phase of the tidal currents (ca. 3–4 h during spring tides) (Bruno et al., 2002; Vázquez et al., 2008). Once subcritical conditions ($G^2 < 1$) are reached over the Sill, almost at the beginning of the eastward phase of the tidal current, this internal bore and its rear undulations are released toward the Alboran Sea.

In the Strait of Gibraltar, the internal solitons mainly propagate eastwards to the Alboran Sea (e.g., Izquierdo et al., 2001; Vlasenko et al., 2009; Álvarez et al., 2019; Dessert et al., 2022) from their release location at CS (Apel, 2000). Their phase speed changes depending on the environmental conditions, such as vertical density stratification, easterly-westerly winds, and (tidal) currents. Sannino et al. (2004) observed, from a three-dimensional model, the maximum phase speed between Tarifa and Pta. Cires (2.5 m s^{-1}) was in agreement with the results of Izquierdo et al. (2001) from a two-dimensional model. Sánchez-Garrido et al. (2008) assessed a maximum speed of up to 2.6 m s^{-1} over the TN from a theoretical approximation. As can be observed in Fig. 1, when they enter the Alboran Sea they radiate as curved wavefronts from diffraction and tidal advection processes (e.g., La Violette and Arnone, 1988; Watson and Robinson, 1990; Apel and Worcester, 2000). Within the Alboran Sea, different fronts have been distinguished using remotely-sensed sea surface roughness and Chlorophyll-*a* (Chl-*a*) surface distribution (Vázquez et al., 2009; Chioua et al., 2013; Navarro et al., 2018). The presence of internal solitons within the Alboran Sea has been found up to 200 km eastward (Pistek and La Violette, 1999; Apel and Worcester, 2000) and up to 50 h after their release from CS.

Nevertheless, these wave packets propagating eastwards through the Strait are not the sole type of observed waves in the eastern Strait of Gibraltar and Alboran Sea areas. Watson and Robinson (1990) distinguished the A-Waves, coming from CS, from another wave packet generated on the Moroccan coast, the O-Waves, which propagates northwards at a slower speed. Although these authors pointed out that these O-Waves appeared frequently, they had not previously been studied and to the best of our knowledge, their exact generation place has not been clarified.

In terms of physical-biological implications, the observed vertical isopycnal displacements over the Sill (even higher than 200 m; Morozov et al., 2002) with semi-diurnal frequency, enhance vertical mixing as a consequence of internal wave breaking (e.g., Wesson and Gregg, 1994; Macías et al., 2007; Ramírez-Romero et al., 2012), leading a nutrient uplifting into the upper Atlantic layer (Bartual et al., 2011; Sala et al., 2022). Such implications have widely been studied from in-situ measurements (e.g., Echevarría et al., 2002) and satellite imagery (Vázquez et al., 2009). These studies have shown that Chl-*a*-enriched coastal waters to the north and south from CS are advected to the center channel as a result of suction which is induced by the mass divergence zones created by internal waves (Macías et al., 2008). After the internal solitary waves have been released from CS, the Chl-*a* is tidally driven as pulses toward the Alboran Sea (Macías et al., 2006; Vázquez et al., 2009; Bartual et al., 2011).

Although the internal wave activity over the continental slope (100 m isobaths delimiting the outer limit of the continental shelf) has important implications in terms of biological or sediment processes (e.g., Lamb, 2014), there are very few studies where the role of the internal activity was previously assessed in this area (e.g., Puig et al., 2004). However, additional model efforts are needed to explore such implications over the coastal domain (Sánchez-Garrido et al., 2015). Finally,

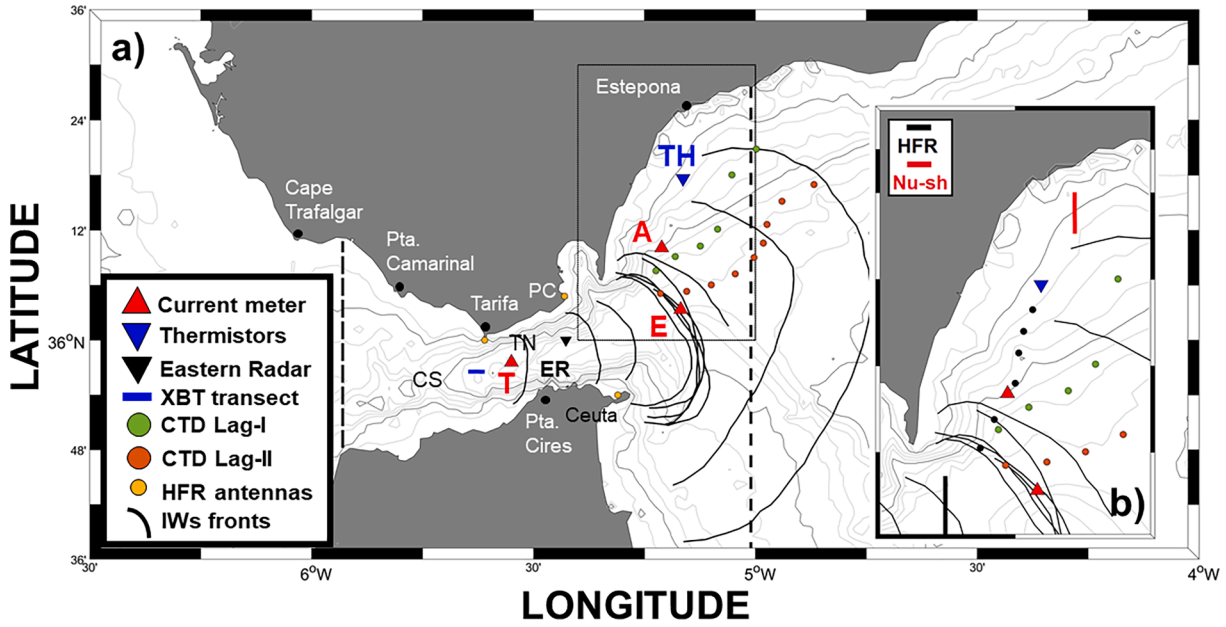

Fig. 1. (a) Map of the study area along with the main geographic locations and the location of the data analysed in the study (see Table 1). Black bold dotted lines show the domain (western and eastern open boundaries) of the UCA3D model. The black dotted rectangle shows (b) zoom of the easternmost Strait and the northwestern Alboran Sea. Black dots are the positions evaluated in Table 4. The grey contour lines represent the bathymetry of the area: the thick contours indicate the 100, 500, and 1000 m isobaths. The thin contours indicate the 200, 300, 400, 600, 700, 800, and 900 m isobaths. CS: Camarinal Sill, CTD: Conductivity, Depth, and Temperature; ER: Eastern Radar; HFR: High-Frequency Radar; IWs: Internal Waves; PC: Pta. Carnero; TN: Tarifa Narrows.

events of internal wave activation or inhibition over CS have also previously been related to subinertial flows (e.g., Vázquez et al., 2008; Ramírez-Romero et al., 2014). This scale of variability is known to be induced by atmospheric forcing and is mainly associated with the variation of the Mean Sea Level Pressure (MSLP) over the western Mediterranean (Candela et al., 1989) and local wind over the Alboran Sea. Moreover, atmospheric forcing also contributes to the previously mentioned (sub)mesoscale processes that characterize the NW-Alboran Sea (e.g., Bolado-Penagos et al., 2021), i.e.: Atlantic jet location, cyclonic and anticyclonic activity, and coastal upwelling extension.

The goal of this study is to answer three main questions related to the internal waves released from the CS: how often are internal waves observed throughout the Strait of Gibraltar? Do these internal waves reach the continental shelf and slope of the NW-Alboran Sea? If so, how long do they take to arrive onto the Alboran shelf and slope? To this aim, the possible fortnightly variability in both their presence and amplitude as well as the effects of subinertial variability are also explored. Likewise, the effects of these internal wave events on the high phytoplankton productivity of these slope waters are considered.

The paper is organized as follows. In section 2, the aspects related to the data and the methodological approach are described. Section 3 describes the identification of the solitons and their travel times from in situ data and numerical modelling. In section 4, an analytical approach to these travel times is depicted. The results of the former sections are discussed in section 5; and finally, the main conclusions are presented in section 6.

2. Data and methodology

To assess the internal soliton activity within the main channel of the Strait of Gibraltar and in the Alboran Sea, different methodological approaches are considered. The used data proceed from multiple sources: (i) time series of current from Acoustic Doppler Current Profilers (ADCP), both moored and vessel-mounted (VM-ADCP), and surface current from High-Frequency Radar (HFR); (ii) temperature records from eXpendable BathyThermograph probes (XBT), thermistors chain, and Conductivity, Temperature, and Depth (CTD) casts; and (iii) numerical modelling.

2.1. Observations

2.1.1. In-situ observations

The in-situ observations used in this study have been collected during different periods of time. The first data were collected during April and May 2003 from two mooring lines of current meters (RCM, Recorder Current Meter). These RCM were equipped with temperature sensors, and they were deployed near Tarifa Point and in the eastern exit of the Strait. The information related to these time series, previously used by Sánchez-Garrido et al. (2008) to evaluate the internal soliton propagation along the main channel of the Strait, is presented in Table 1. For the Tarifa mooring (T, red triangle in Fig. 1a) the records of the current meters at 90 m and 140 m (T3 and T4, respectively in Table 1) were analysed. For the mooring line E at the east of the Strait (E, red triangle in Fig. 1a), the current meters 60 m, 90 m, and 120 m depth (E1, E2, and E3, respectively in Table 1) were assessed. The E1 time series is shorter in length due to instrumental malfunctioning.

In November 2003, simultaneous profiles of XBT temperature and VM-ADCP current velocity were collected on-board the Research Vessel (R/V) *"Mytilus"*, while it crossed an internal soliton train propagating eastwards near Tarifa (horizontal blue line in Fig. 1a). These observations, in conjunction with a short time series from a moored ADCP (in October 2011) close to the easternmost mouth of the Strait (A in both Fig. 1a and Table 1), support the identification of internal solitons in the area.

Additionally, temperature time series have been recorded by a thermistor chain moored over the NW-Alboran Sea continental slope between September and October 2015 (TH, inverted blue triangle in Fig. 1a and Table 1), at a depth of 150 m. The mooring consisted of 35 temperature sensors (S2T600 autonomous data logger, NKE-Instrumentation) placed every 3 m, with ± 0.05 °C accuracy, which measured the water column from 38 m (first thermistor) to 140 m depth (last thermistor).

During the time the thermistors were moored, an oceanographic shipborne sampling campaign was conducted (on board the R/V *"Sarmiento de Gamboa"*). A total of fifteen CTD casts were carried out (Table S1). These profiles (North Western-Alboran, NW-A-x) were collected on September 25 and 26, 2015 (NW-A I, green dots) and October 2 and 3, 2015 (NW-A II, orange dots). The CTD casts positions were chosen according to the trajectories followed by two Lagrangian drifters released within the Strait.

To detect the arrival of internal waves over the NW-Alboran Sea, CTD casts were also conducted by an undulating Nu-shuttle platform. The Nu-shuttle is a towed undulating instrument for the characterization of the water column and it incorporated CTD profiles. These measurements (1-second interval sampling) were carried out on board the R/V *"Sarmiento de Gamboa"* in October 2008 (Vázquez et al., 2009). The perpendicular transect (36.35 – 36.40° N, 5.12° W; red vertical line in Fig. 1b) was sampled during spring tides (new moon on October 1, 2008) from 15:01 to 15:20 UTC and was performed from offshore (200 m isobath) to the coast (60 m isobath). From the isobaths 200 to 100 m the Nu-shuttle was dragged at a constant depth of 55 m and when it reached 100 m bathymetry, it was positioned at approximately 35 m depth, maintaining this depth until the end of the transect.

2.1.2. High-frequency radar system

The intensity of the Atlantic inflow which enters the Alboran Sea was evaluated from the HFR system located near the easternmost exit of the Strait of Gibraltar. Different studies have previously validated and implemented this methodology in the area (e.g., Soto-Navarro et al., 2016; Lorente et al., 2019). The HFR system consisted of a three-site shore-based CODAR (Coastal Ocean Dynamics Applications Radar) Seasonde network installed in Ceuta, Pta. Carnero and Tarifa (yellow circles in Fig. 1a), but since February 2019, the system has had a fourth antenna located in Pta. Camarinal. Nevertheless, this work does not take

Table 1
Summary information about the moorings. T, E, and A are the current meters moored in Tarifa and in the east of the Strait of Gibraltar, respectively (red triangles in Fig. 1). TH corresponds with the thermistors mooring (inverted blue triangle in Fig. 1).

Mooring name	Position		Acquisition time			Depth (m)	Sampling interval
	Latitude (°N)	Longitude (°W)	Start time (UTC)	End time (UTC)	# days		
T3	35.96	5.55	29.Apr.2003–14:43	22.May.2003–23:02	22	90	2′
T4			29.Apr.2003–14:43	22.May.2003–23:02	22	140	2′
E1	36.06	5.17	01.May.2003–09:32	13.May.2003–09:16	12	60	2′
E2			01.May.2003–09:32	22.May.2003–23:02	21	90	2′
E3			01.May.2003–09:32	22.May.2003–23:02	21	120	2′
A	36.17	5.21	11.Oct.2011–13:49	12.Oct.2011–12:50	1	14	2′
TH	36.29	5.16	08.Sep.2015–09:09	08.Oct.2015–11:49	30	38–140	1′

into account data from the antenna located in Pta. Carnero. The central frequency of the antennas is 26.8 MHz, and they have a 150 KHz bandwidth, providing coverage up to 40 km from the coast (Soto-Navarro et al., 2016). In this study, the hourly dataset is used which is freely available from the *Puertos del Estado* OpenDaP (Open-source Project for a Network Data Access Protocol). Data were analysed during September-October 2015 along a transversal transect to the Strait (from 36.00 to 36.07° N, 5.30° W, black vertical line in Fig. 1b). The hourly data were low pass filtered with a 30-hour cut-off to retain the subinertial surface flow variations.

2.1.3. Satellite imagery

The presence of internal waves over the shelf of the Alboran Sea has been evaluated from an ASAR (Advanced Synthetic Aperture Radar) image collected by an active radar sensor aboard the European Space Agency (ESA) satellite ENVISAT. These images have been previously used in the same area to detect the presence of the fronts from the sea surface roughness (e.g., Vázquez et al., 2009; Chioua et al., 2013; Navarro et al., 2018).

To analyse the oceanic productivity associated with internal wave events, daily Level-3 surface Chl-*a* concentration (mg m^{-3}) images (4-km resolution) from MODIS (Moderate Resolution Imaging Spectroradiometer) were downloaded from the NASA Ocean Color Website (http://oceancolor.gsfc.nasa.gov).

2.1.4. Atmospheric variables

Variations in both MSLP over the western Mediterranean Sea and local wind over the NW-Alboran Sea, at 10 m height, were analysed during the time periods that the moorings were deployed (Table 1) to characterize the atmospheric forcing. Hourly remote and local atmospheric forcing data were downloaded from the ERA5 reanalysis (0.25° x 0.25°) data that are archived in the European Centre for Medium-Range Weather Forecasts (ECMWF, https://cds.climate.copernicus.eu) (Hersbach et al., 2023).

2.2. Tidal current prediction over Camarinal Sill

The tidal current prediction was obtained applying a least squares harmonic analysis on a long-term current velocity time series (ca. 6 months) acquired by an ADCP over CS spanning the depth range 45–265 m (see Fig. 1a for location). This mooring was deployed from October 1994 to April 1995 as part of the Strait 94–96 Experiment (Vázquez et al., 2006).

To identify when an internal wave event is expected to be generated and obtain an approximate time for the release of the waves from CS, we computed internal time series for G^2 (Eq. (1)). Using the predicted tidal current profiles over CS, we were able to predict G^2 values by assuming (i) that the AMI interface depth coincides with the depth of the maximum vertical shear of horizontal current (Tsimplis and Bryden, 2000), and (ii) characteristic density values for the upper and lower layer of $\rho_1 = 1027.00$ kg m^{-3} and $\rho_2 = 1028.50$ kg m^{-3}, respectively (Bray et al., 1995).

2.3. UCA3D model

Numerical simulation by the hydrodynamic model UCA3D supports the analysis of the main behaviour of the internal solitons generated in the Strait of Gibraltar that are part of our observations. It is a 3D, non-linear, baroclinic, non-hydrostatic model in Cartesian coordinates and sigma-levels (Álvarez et al., 2011). The model simultaneously solves the three-dimensional and two-dimensional (depth-averaged) primitive equations for an incompressible and rotating fluid.

The grid domain covers the Strait and the NW-Alboran Sea (from 35.21 to 36.51° N, from 5.01 to 5.93° W), with a horizontal resolution of 100 × 100 m/500 × 500 m (Δx and Δy, respectively) and 50 sigma-levels (N_σ) in the vertical direction. At the open boundaries, a radiation condition, written in terms of the deviations of tidal elevation and tidal velocity from their observed values, was employed to ensure the propagation of disturbances away from the model domain. The horizontal eddy viscosity coefficient is $K_0 = 0.05$ m^2 s^{-1}, and the time step for integration is 2 s. Bottom friction is parameterized with a standard bottom-drag coefficient $C_D = 0.003$ and a bottom roughness parameter $z_0 = 0.001$ m. The model was forced at the western and eastern open boundaries (Fig. 1a) with an M_2 tidal wave and a steady baroclinic exchange based on constant mean Atlantic and Mediterranean mean flows of 1.19 Sv (directed to the east) and 1.14 Sv (directed to the west) (García-Lafuente et al., 2002b). A complete description of the model, including governing equations and values of the parameters used, can be found in Álvarez et al. (2011) and González et al. (2013).

3. Identification of solitons and observed travel times

The presence of internal solitons and the travel time they spend between their release over CS and the arrival at the Alboran Sea were analysed from the in-situ data as well as numerical modelling outputs.

Fig. 2 shows the presence of a soliton from a vertical section of temperature along with current velocity (vector field) profiles recorded by a VM-ADCP. Here an internal soliton train (Fig. 2b) can be observed moving eastward through the Strait of Gibraltar (XBT, horizontal blue line in Fig. 1a). As part of the sampling process, the vessel followed the fronts of the internal waves, positioning itself ahead of them. Once the first front was passed, the vessel altered its course and moved towards the fronts, crossing them while the XBTs were deployed. As a result, the wavelengths obtained from these measurements are only apparent and need to be corrected for the relative motion of the waves concerning the vessel.

To correct this effect, the apparent horizontal distances were multiplied by the ratio $(V_v + c_w)/V_v$, where V_v denotes the velocity of the vessel and c_w represents the propagation speed of the waves. In this case, the values used were $V_v = 2.5$ m s^{-1} and $c_w = 1$ m s^{-1}, which resulted in a ratio of 1.4. Consequently, the true wavelengths were 1.4 times longer than the apparent ones.

This fact is revealed by the undulations of the isotherm's depths, which descend to deeper vertical positions with the arrival of the depression soliton. Taking a value of 14.50 °C as the characteristic temperature of the AMI water, the leading soliton shows an amplitude of 120 m.

Looking at the tidal current prediction (Fig. 2a), and following the empirical prediction method described in section 2.2, this internal soliton train may have been generated during the previous westward phase of tidal current (-1 m s^{-1} is reached at 11:00 UTC on November 12, 2003) and released from CS at approximately 15:00 UTC. Therefore, its transit from CS to the easternmost position of the measurement transect lasted ca. 3.00 h. The soliton-induced current in the upper layer was stronger over the leading edge of the troughs than over the crests. This is the basic feature that allows the detection of soliton from current velocity observations in the layer above the pycnocline within the study area (Vázquez et al., 2006).

Based on the premises established in the previous paragraphs, the methodology used to identify the internal wave solitons at the observation sites was mainly focused on the tracking of the A-Waves generated around CS at the observation sites (see locations in Fig. 1). After revising some general considerations of internal solitons in the current and temperature fields, the methodological aspects for the 2003 and 2011 data were differentiated. The results are based on the current velocity records collected at T-E, and A moorings, respectively, from those of the September - October 2015 data, which were based on the temperature records of the TH mooring and HFR-derived observations on the eastern side of the Strait.

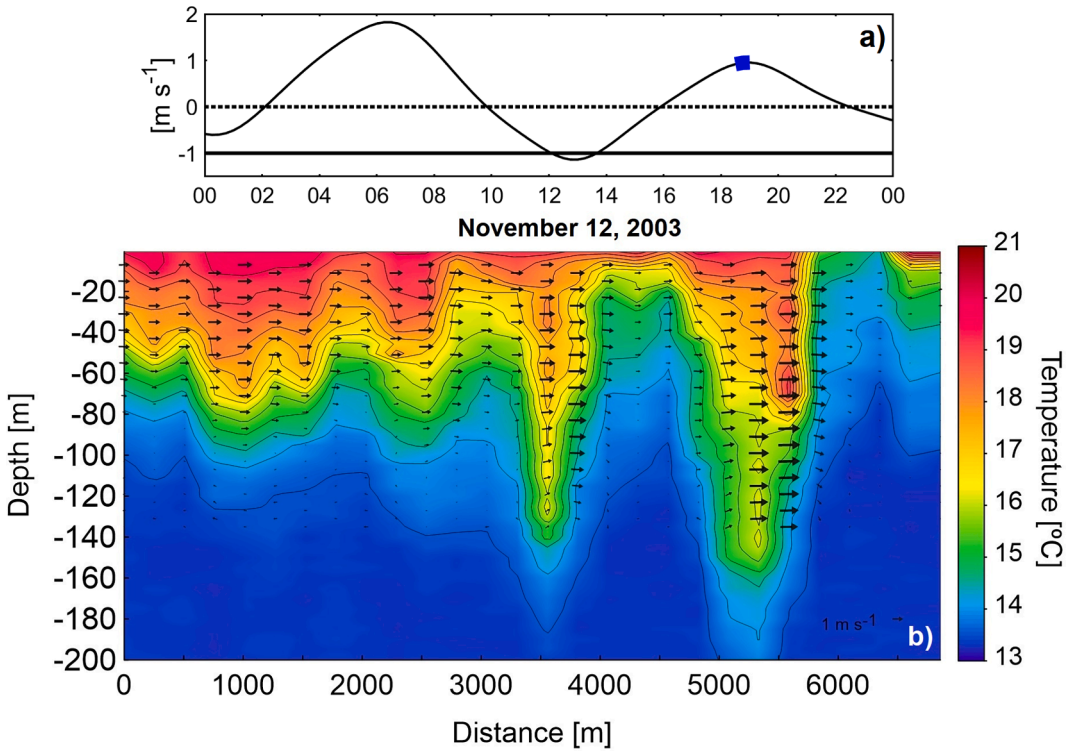

Fig. 2. (a) Hourly tidal current prediction (m s^{-1}) over Camarinal Sill (CS) at 45 m depth. The horizontal black dotted line delimits the positive/negative current directed toward the Mediterranean/Atlantic side. The horizontal black bold dashed line indicates the 1 m s^{-1} westward tidal current. The blue mark indicates the time of the XBT transect deployed near Tarifa (blue horizontal line in Fig. 1a). (b) Vertical section of temperature (°C) from XBTs following an internal soliton train moving eastward through the Strait of Gibraltar. Temperature is superimposed by the velocity profiles recorded (black arrows). 0 (km) corresponds with CS location. (For interpretation of the references to color in this figure legend, the reader is referred to the web version of this article.)

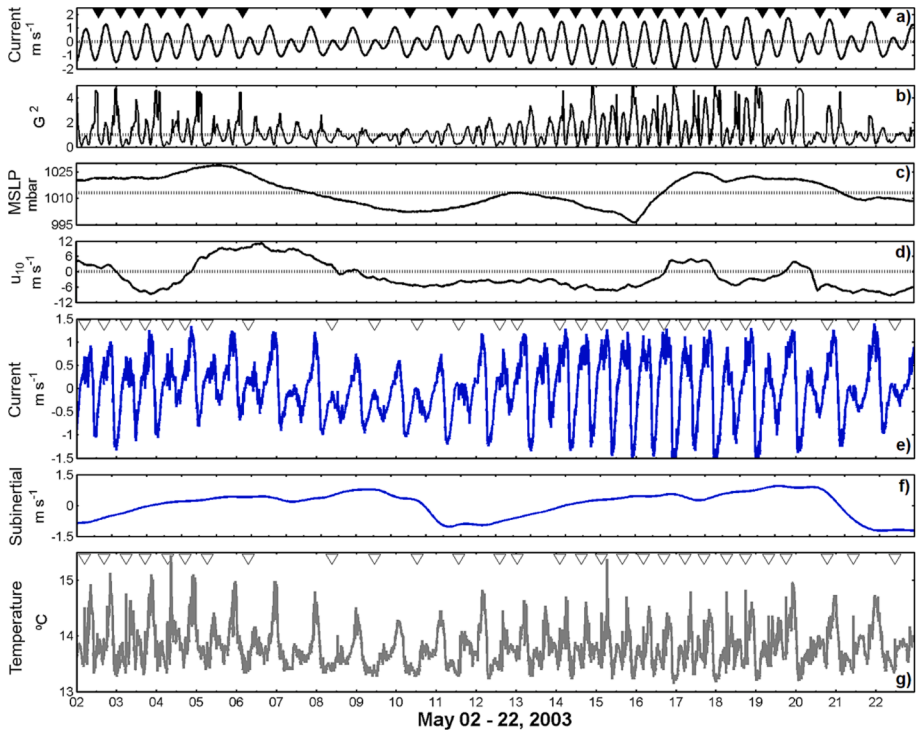

Fig. 3. (a) Tidal current prediction (m s^{-1}) over Camarinal Sill (CS) at 45 m depth. The horizontal black dotted line delimits the positive/negative current directed toward the Mediterranean/Atlantic side. (b) Internal Froude number (G^2) estimation based on (a). The horizontal black dotted line delimits critical conditions ($G^2 = 1$). (c) Temporal evolution of the Mean Sea Level Pressure (MSLP, mbar) over the western Mediterranean Sea. The horizontal black dotted line delimits the high/low MSLP (1013 mbar). (d) Temporal evolution of the zonal component of the wind at 10 m height (u10, m s^{-1}) over the Alboran Sea. The horizontal black dotted line delimits the direction of the wind: positive/negative from west/east. (e-g) Time series of the zonal current speed (e, m s^{-1}), subinertial zonal component of the current (f, m s^{-1}), and temperature (°C) recorded in Tarifa at 90 m depth (T3 in Table 1). Black inverted triangles in (a) indicate the release of internal solitons over CS ($G^2 <$ 1). White inverted triangles in (e) and (g) indicate the arrival events of the solitons at the mooring T3. Information about the times is detailed in the supplementary material (Tables S2 and S3). Time units in the x-axis are days.

3.1. From the in-situ data: The journey from Camarinal Sill to the easternmost Strait of Gibraltar

3.1.1. May 2003

Figs. 3 and 4 show the time series of zonal current intensity and temperature recorded at the moorings T and E, respectively, located 35.93 km apart, along with the MSLP averaged over the Western Mediterranean Sea and the zonal wind velocity component at 10 m averaged over the Alboran Sea. Semidiurnal internal tides are evident in both variables (e and g) which are responsible for the main oscillations. In addition, the existence of secondary large peaks of higher frequency (in current intensity and temperature) is indicative of the arrival of the internal solitons at the mooring emplacements. These peaks seem to be larger and more frequent during spring (new and full moon on May 1 and 16, 2003, respectively) than during neap tides (first and later quarter moon on May 8 and 23, 2003, respectively) at all the measured depths (T*n* and E*n* in Table 1).

Therefore, the internal soliton behaviour is quite different between spring and neap tides. While during spring tides the oscillations are detected both in current speed and in temperature, their identification during neap tides is relegated to a few events during every semidiurnal cycle. These neap tide events are controlled by the diurnal inequality, which is present in both tidal current prediction (Fig. 3a and 4a) and measured zonal current (Fig. 3g and 4 g).

To assess the travel time of the internal solitons from their release location (CS) to the T and E moorings, we have identified soliton arrivals following the methodology illustrated in Fig. 5, where two events of A-Wave generation occurred. The releasing time of solitons from CS (R_{CS}) has been estimated following the empirical model described by Vázquez et al. (2008) (i.e., westward tidal current reaches 0.6 m s^{-1}). Table S2, in the supplementary material, summarizes the information about these events.

The released internal waves are recognized at T mooring (M_T) (18.52 km apart, T3 current meter), by the short-period oscillations of both temperature and zonal current velocity at 90 m depth, 3.30 and 3.43 h after their release from CS for the first and second events, respectively (Fig. 5c-d). These internal waves are observed at the E mooring (M_E, 54.45 km apart) 5.75 and 5.40 h later after they leave the T mooring.

On average, the solitons took 4.50 h to reach the T mooring (from CS), but the travel time differs, however, between spring and neap tides. During spring tide, it was shorter, ca. 4 h. Whereas during the neap tide, it was significantly longer, ca. 6.50 h. This marked difference in the travel times seems to be related to the lower eastward current maxima during the analysed neap tides, which was in the range of 0.40–0.60 m s^{-1}. Regarding the mean travel time between moorings T and E (35.93 km apart), it was 6.30 h, which means that they move at an average speed of 1.56 m s^{-1}. However, this varies between spring (ca. 6.00 h)

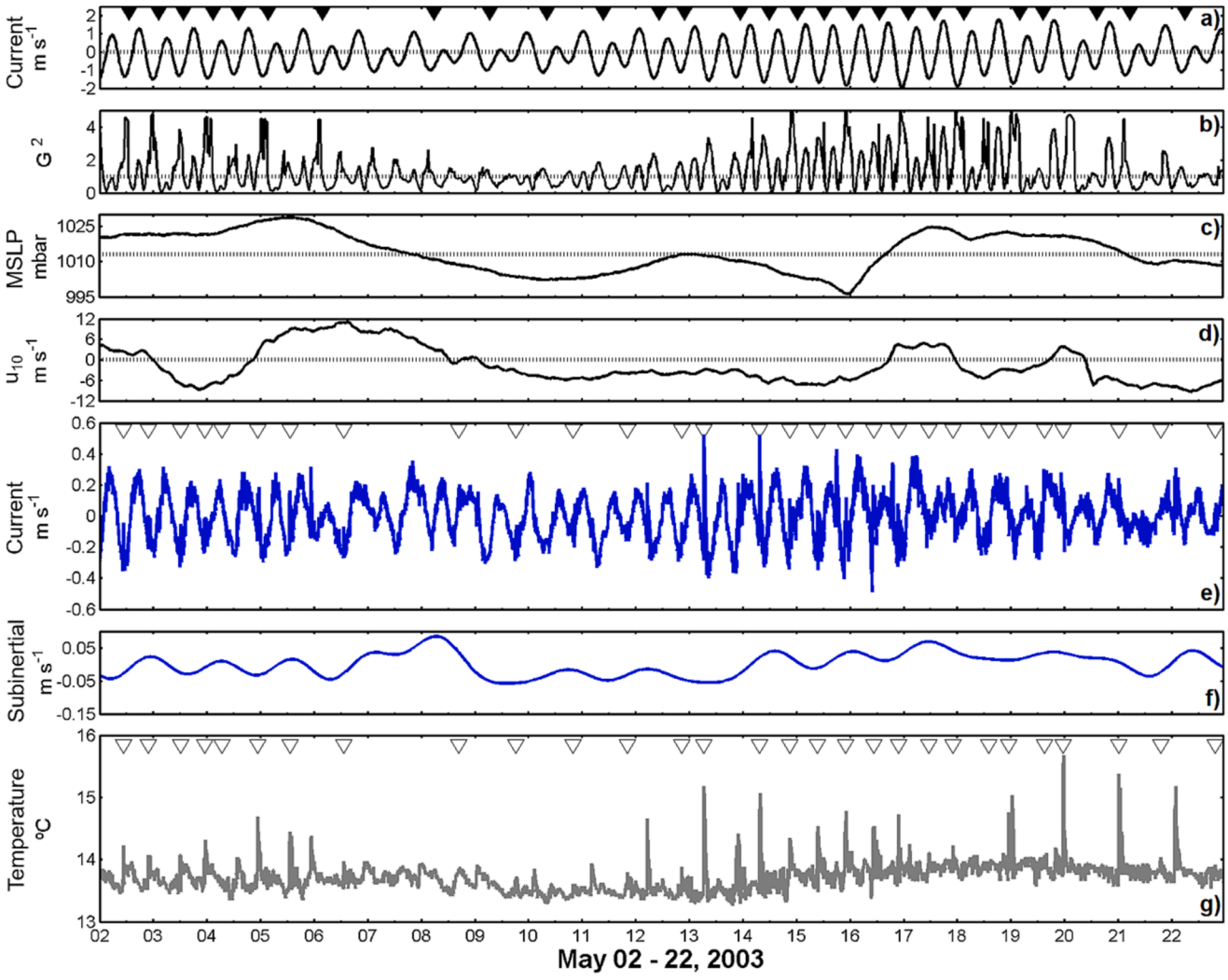

Fig. 4. (a-d) The same as Fig. 3. (e-g) Time series of the zonal current speed (e, m s^{-1}), subinertial zonal component of the current (f, m s^{-1}) and temperature (°C) recorded in the east of the Strait of Gibraltar (E in Fig. 1a) at 120 m depth (E3 in Table 1). Time units in the x-axis are days.

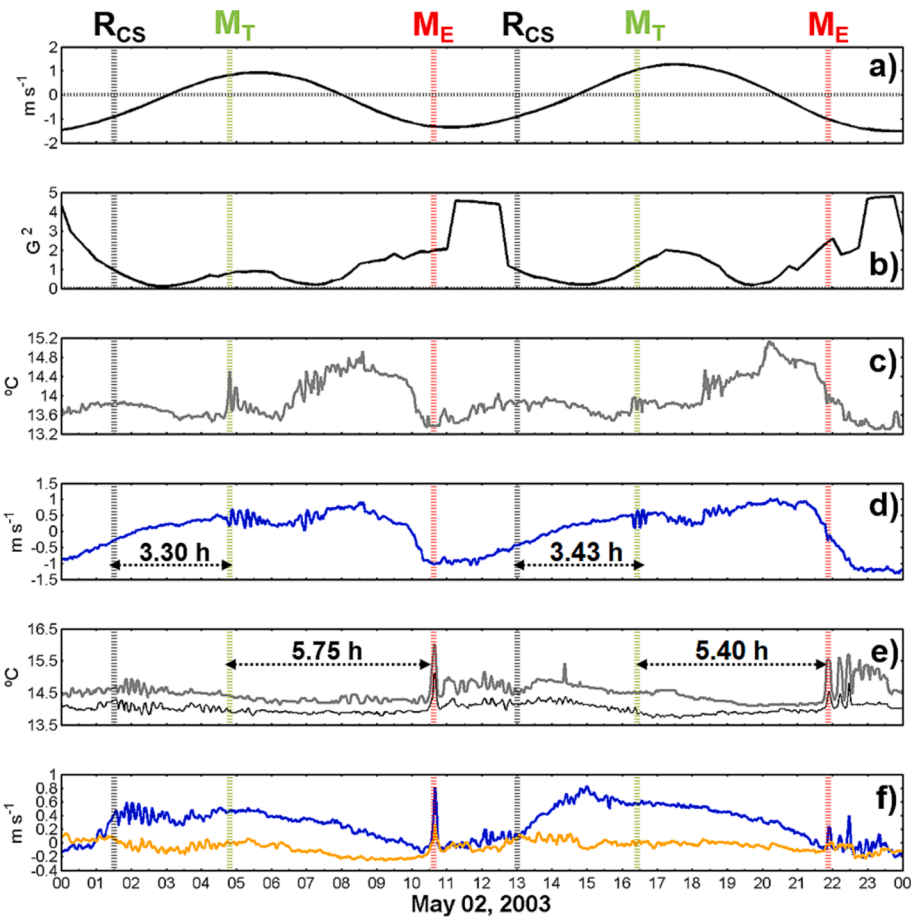

Fig. 5. Time series of the different variables used in the identification of internal solitons when passing by the moored lines deployed at Tarifa (T) and the east of the Strait (E) sites (see Fig. 1a). (a) Tidal current prediction over Camarinal Sill (CS) (m s^{-1}). The horizontal black dotted line delimits the positive/negative current directed toward the Mediterranean/Atlantic side. (b) Internal Froude number (G^2) estimation based on (a) data. (c) and (d) temperature (°C) and eastward current (m s^{-1}), respectively, at T3 current meter (90 m depth) of mooring T; (e) temperature (°C) at current meters E1 (60 m depth, grey) and E2 (90 m depth, black) of mooring E. (f) East (blue) and north (orange) current speed (m s^{-1}) at current meter E1 (60 m depth). R_{CS}: releasing time of solitons from CS; M_T: arrival times of solitons at mooring T; M_E: arrival times of solitons at mooring E. The dashed black horizontal double arrows indicate the elapsed time between the release from CS and the arrival at T and E moorings. Time units in the x-axis are days. (For interpretation of the references to color in this figure legend, the reader is referred to the web version of this article.)

and neap tides (ca. 8.00 h). Table S3, in the supplementary material, summarizes the information about these events.

3.1.2. October 2011

Fig. 6 shows the record of the zonal component of the current velocity at 14 m depth, sampled at 2-minute intervals (black line) during spring tides (full moon on October 12, 2011). This ADCP was slightly moored northeast of the Strait of Gibraltar (at 45 m depth) (see A location in Fig. 1a). The filtered zonal current velocity is depicted, as superimposed, after removing the signals of periods shorter than 1 h (red line). Two events of internal soliton arrival at the mooring place A (black arrows) can be identified during this time interval by the associated large amplitude oscillations of the current velocity (up to 1 m s^{-1}) that they produce. It is worth noting that, due to the asymmetry of the soliton-induced horizontal current (with a larger eastward increase than its subsequent decrease), there is a bias in the filtered time series, i.e., an increased eastward current, during the time lapse in which the solitons were crossing the measurement site. This behaviour allows the identification of the internal soliton signals even in time series recorded at low sampling rates, such as the hourly surface current time series provided by the HFR antennas deployed in the eastern Strait of Gibraltar, as shown in the following section.

3.2. From the Strait of Gibraltar to the Alboran Sea

In this section, we analyse solitons during the period from September to October 2015 from both surface current velocity observations (acquired by the HFR system in the Strait of Gibraltar) and the seawater temperature record onto the NW Alboran Sea slope (TH in Fig. 1a).

Again, the release times from CS (inverted black triangles in Fig. 7a)

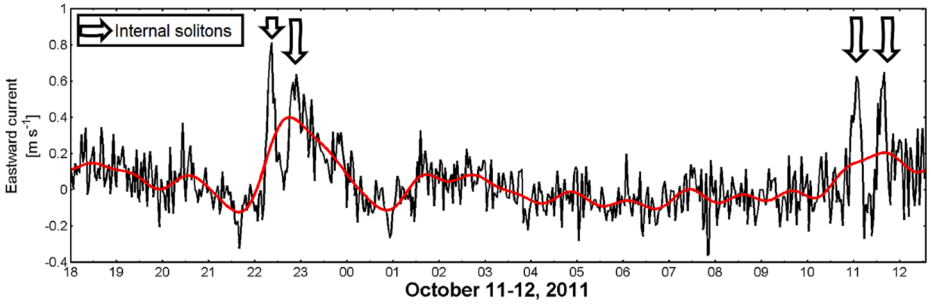

Fig. 6. Time series of the zonal current at 14 m depth recorded by an ADCP at location A (see the map of Fig. 1b). The black line is the original record at a 2-minute sampling rate, while the red line is the filtered series after removing the signal of periods shorter than one hour. (For interpretation of the references to color in this figure legend, the reader is referred to the web version of this article.)

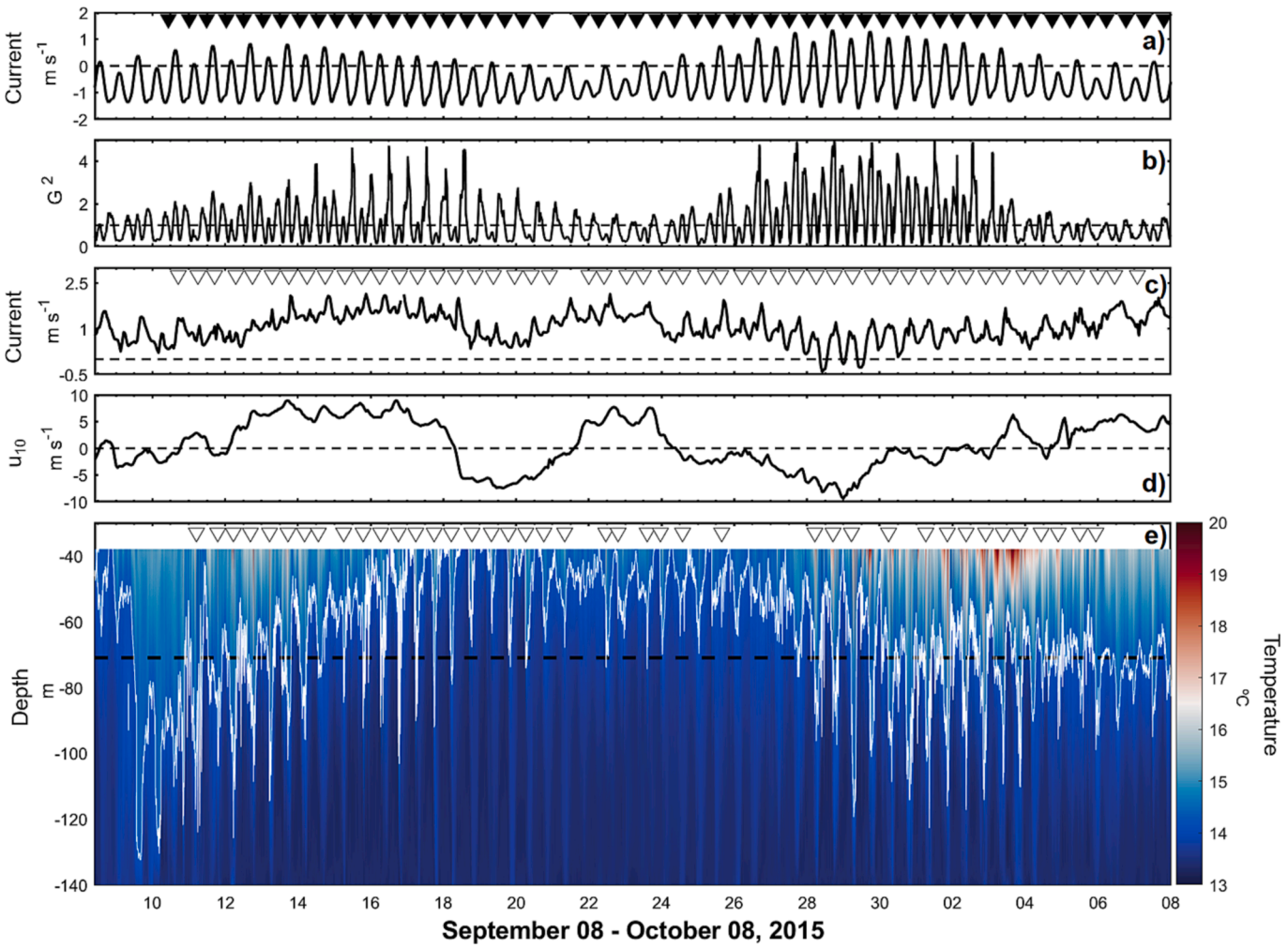

Fig. 7. Temporal evolution of (a) tidal current prediction (m s^{-1}) over Camarinal Sill (CS). (b) Internal Froude number (G^2) estimation based on moored data over CS. (c) Temporal evolution of the hourly zonal component of the current (m s^{-1}) in ER location (Fig. 1a). The horizontal black dotted line delimits the positive/negative current directed to the east/west. White inverted triangles denote the dates when internal solitons reach ER (Fig. 1a). (d) Zonal component of wind at 10 m height (m s^{-1}) over the Alboran Sea. The horizontal black dashed line in (a) and (c) delimits the positive/negative current directed toward the Mediterranean/Atlantic side, in (b) the horizontal black dashed line delimits critical conditions ($G^2 = 1$), and in (d) the zero reference that delimits the positive/negative wind direction to the east/west. (e) Vertical variability of the temperature (°C) from the thermistor chain deployed at TH (Fig. 1a). The white line marks the position of the Atlantic/Mediterranean Interface at 14.20 °C. The black dashed horizontal line indicates the average position of the interface (~70 m). White inverted triangles denote the dates when internal solitons reached the TH mooring. Information about the times is detailed in the supplementary material (Table S4).

and the internal Froude number (Fig. 7b) are analysed to estimate the soliton's travel time from CS to ER and TH points (more detailed information about these events on Table S4). Despite the relatively low time resolution of the HFR records (1 h), we were able to identify the presence of solitons (Fig. 7c). As explained above (Fig. 6), this was possible due to the asymmetry of the perturbation in the horizontal current velocity (intensification of eastward current) that provokes the passing of the internal solitons. According to CS tidal current prediction, for this period, differences in arrival times between spring and neap tide events were smaller than in the previous case. While the solitons reached the ER radar point (30 km apart) after ca. 5 h during spring tides, they would take ~ 5.40 h during neap tides (Table S4).

The arrival of solitons at the TH mooring (70.46 km apart) displays a consistent regularity as can be observed in Fig. 7e. These solitons are identified along the isotherm (white line in Fig. 7e) which corresponds to the AMI in this area and by this time of the year. According to previous studies, the AMI is related to a salinity of 37.30 and, a temperature of 14.20 °C (Temperature and Salinity diagrams -from CTDs detailed in Table S1- are shown in Figure S1).

The temperature profiles showed drastic warming of the upper water layer as well as the sinking of the AMI below 90 m depth (from September 30th until October 8th) (Fig. 7e). Throughout these days, the zonal component of the wind (Fig. 7d) showed values lower than, or close to, zero, which corresponds with winds directed to the west (negative zonal wind). The shallowest positions of the interface were observed from September 16th to 27th, when the 14.20 °C isotherm was displaced up to the depth of the first thermistor (38 m depth). This shallowest position of the interface was related to the presence of eastward winds (positive zonal wind, Fig. 7d).

Regarding the travel time of the solitons from ER (Fig. 7c) to TH (Fig. 7e) there were no considerable differences between spring and neap tides (Table S4). Solitons took an average of (11.07 ± 1.40) h from ER to TH (40.76 km apart).

For the sake of clarity, Fig. 8 shows an example of how identification and tracking of the internal solitons were carried out during the September – October 2015 analysis period at ER (Fig. 7c). The internal solitons are tracked at ER location (black triangle in Fig. 8a-b) by identifying the high current pulses left by the passing of internal solitons in the HFR-derived surface current maps.

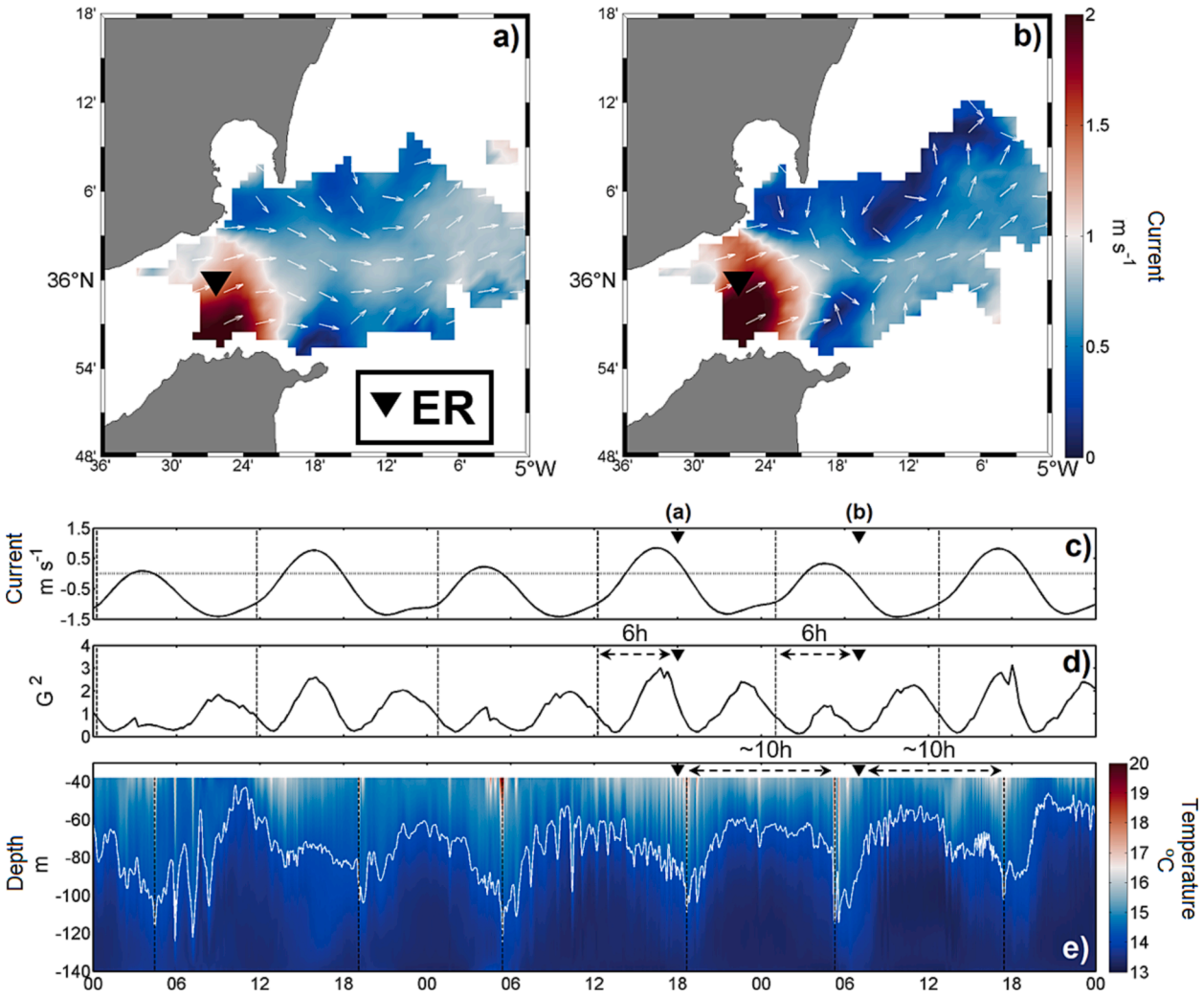

Fig. 8. (a) Surface current speed map for September 12, 2015, 18:00 UTC. (b) Surface current speed map for September 13, 2015, 07:00 UTC. (c) Tidal current prediction over Camarinal Sill (CS) (m s^{-1}). The horizontal black dotted line delimits the positive/negative current directed toward the Mediterranean/Atlantic side. (d) Internal Froude number (G^2) estimation based on moored data over CS. (e) Vertical variability of the temperature (°C) from the thermistor chain deployed at TH (see Fig. 1). The white line marks the position of the Atlantic-Mediterranean Interface (AMI) at 14.20 °C. Vertical dotted black lines in (c) and (d) indicate the predicted time for internal solitons release from CS ($G^2 < 1$), and (e) indicates the arrival of solitons at the TH mooring that is identified by the sharp depressions of the AMI interface. Inverted black triangles in (c-e) mark the time location of the maps (a-b).

3.3. Solitons from modelling

As previously introduced, the most likely origin of the internal solitons recorded at TH mooring (see the map of Fig. 1a) are those corresponding to the A-Waves, generated around CS and propagating eastwards along the Strait of Gibraltar; and the O-Waves, generated off the Ceuta coast and propagating northwards.

In this section, we present the results of the simulations from the UCA3D model to further explain the behavior of the internal solitons in the area. Fig. 9 shows the time evolution of the Sea Surface Height (SSH) perturbation and vertical velocity of the AMI induced by the internal waves generated in the Strait of Gibraltar, during a period of eight hours. Apart from the fronts coming from the western side (CS) and propagating eastwards, a second type of front can be identified as generating at the Moroccan slope (indicated by the black unfilled arrows) and propagating northwards, which may be related to the so-called O-Waves.

In Fig. 9a, an internal soliton train (A-Wave) is observed moving eastward after being released from CS. Also, in a location to the north of Ceuta (see the black unfilled arrow), there are registered high vertical velocity values at the AMI interface can be seen together with significant sea level perturbations, which is indicative of internal wave activity (O-Waves). At this point, the eastward component of the zonal barotropic tidal current near that location (embedded small plot in Fig. 9a) shows high values, with the maximum value being reached one hour later.

The internal wave generation of the O-Waves seems to be related to a submarine promontory that is roughly positioned perpendicularly to the Moroccan coast. Therefore, when the eastward tidal current is intensified over the promontory, an internal bore can be formed on the lee side (east of the promontory). This bore may be trapped on that lee side until the eastward barotropic current weakens to values lower than the propagation speed of the internal bore, leading to its release from the lee side of the promontory in a northwest direction. It is worth noting that the bore began to move northwestwards at the time of the Fig. 9b, once the barotropic current is close to zero. At the time of Fig. 9d, the presence of the O-Waves coincides with the arrival of the A-Waves in the middle of the Strait. During the following time steps (Fig. 9f-i) both waves (A and O) continue their propagation into the NW corner of the Alboran Sea. Therefore, it is expected that some of the internal soliton fronts that reach the TH mooring could have a different origin than the A-Waves.

As observed in the HFR-derived surface current field (Fig. 8a-b),

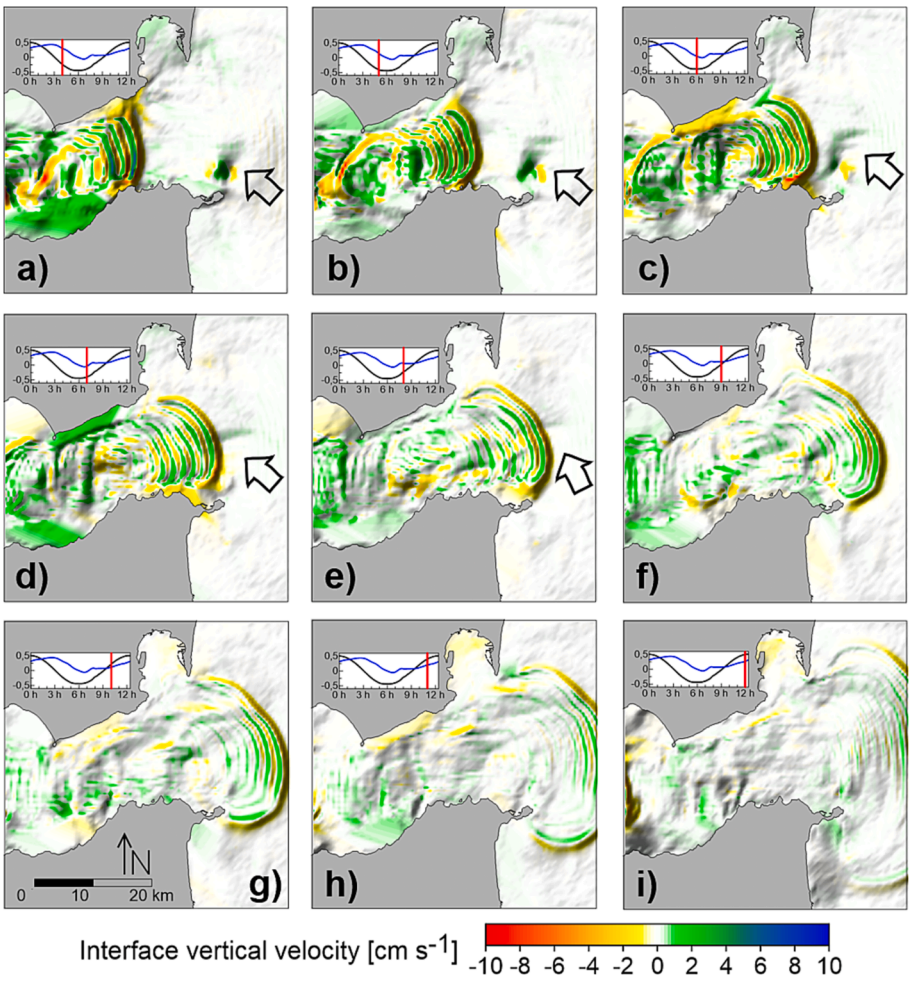

Fig. 9. Sea Surface Height (SSH) manifestation (grey) superimposed to the vertical velocity at the Atlantic-Mediterranean Interface (AMI, colour scale), both created by the tidally generated internal waves in the Strait of Gibraltar simulated by the UCA3D hydrodynamic model. The time of each map is indicated, by a red vertical line, over the embedding of small plots of the time evolution of zonal barotropic current (blue line) and sea surface elevation (black line) near the Ceuta coast. Black unfilled arrows indicate the generation of fronts at the Moroccan slope. (For interpretation of the references to color in this figure legend, the reader is referred to the web version of this article.)

wave signals can also be identified by the horizontal surface current. We simulated the passing of the internal soliton train with the UCA3D model. In this case, we focused on the horizontal surface current simulations after the simulated time series had been time-averaged. This was to remove the signals of periods smaller than 1-hour to resemble the HFR currents maps. Fig. 10 shows these hourly averaged maps superimposed on the map of the sea surface elevation field (without time-averaging), allowing for location tracking of the internal soliton trains. A pulse of high horizontal current intensity was travelling at the rear of these soliton trains. These pulses represent the footprints that the internal-soliton-induced currents leave in the hourly-averaged currents. Therefore, UCA3D results agree with the detection of the arrival of these solitons at the eastern side of the Strait using the HFR-derived surface current maps. As suggested by the maps in Fig. 10d, the ER location at the middle of the Strait is quite appropriate to track the arrival of these pulses on the HFR maps.

Fig. 11 depicts the travel times of the solitons (A-Waves) from CS to the TH mooring from UCA3D. The travel time from the generation place (CS, High Tide –HT + 00 h) to the E mooring is 10 h (HT + 10 h), while it takes 10 h more to arrive at the TH mooring (HT + 20 h). The soliton arrival times are also shown at T mooring (HT + 02 h) and the zone identified as ER (HT + 06 h). Therefore, according to the UCA3D simulations, the internal solitons released over CS would take ~ 20 h to reach the TH mooring location in the Alboran Sea.

4. Analytical approach

To gain a deeper understanding of the physical processes involved in the generation and propagation of the internal solitons, we analysed the internal solitons from an analytical approach. We computed theoretical soliton travel times between the locations described in the previous section exploring how different factors (e.g., atmospheric forcing, the density, and temperature structure of the Alboran Sea) affect the behaviour of the solitons.

4.1. Joint effect of subinertial current and maximum eastward tidal current on the soliton travel times

As mentioned, the internal solitons are released from CS approximately 1.50 h before the reversion of tidal currents from westwards to eastwards in the upper layer. Thus, the eastward tidal current increases while internal solitons are moving eastwards. Below, we describe a simple analytical frame for the effect of how the increased eastward tidal current on the solitons' propagation is explained. To do this, we estimate the mean traveling velocity of the solitons (c_m) in any portion of the channel between CS and the E mooring, concerning a fixed frame as:

$$c_m = c + u_m + \langle \overline{u}_T \rangle \quad (2)$$

where c is the mean non-linear propagation speed of solitons concerning water; u_m is the advection velocity of solitons by the mean upper layer current (where solitons displace), and $\overline{u}_T$ represents the advection due to upper layer tidal current and where the brackets $\langle\ \rangle$ indicate time averaging along the time interval T_s, spent by solitons in traveling the given portion of the channel. The tidal current amplitude, mean current, and slow time variations of the latter vary linearly between CS and E locations (Sánchez-Román et al., 2012). In these conditions, we can

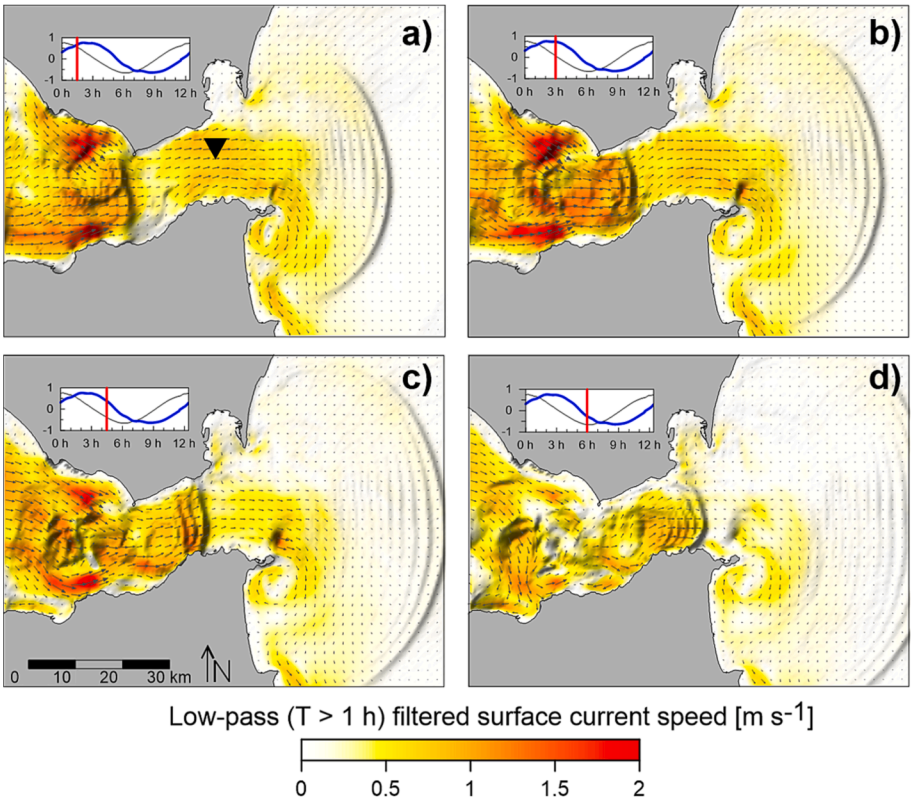

Fig. 10. Simulations of the internal-soliton-induced sea level from the UCA3D hydrodynamic model. The time of each map from (a) to (d) is indicated, by the red vertical line over the embedding small plots of the time evolution of zonal barotropic current after being filtered to remove the signal of periods shorter than 1 h (blue, m s^{-1}) and sea surface elevation (grey, m) over Camarinal Sill at the centre of the channel. The black inverted triangle indicated the position of ER (Fig. 1a). (For interpretation of the references to color in this figure legend, the reader is referred to the web version of this article.)

express $\overline{u}_T$, for instance, between sections CS and ER or between T and E, as:

$$\overline{u}_T = \frac{(U_i + U_f)}{2} cos(\omega t - \delta) \tag{3}$$

where there is no delay in the occurrence of tidal current peaks between the two considered points. U_i and U_f are the tidal current amplitudes at the initial and final points of the solitons' travel, respectively; ω is the angular frequency of the main semidiurnal tidal constituent M_2; and δ stands for the adjustment of the tidal current phase at the starting point. According to the assumed linear variation of tidal current amplitude $U_f = \gamma U_i$, γ being a constant, we can write:

$$\langle \overline{u}_T \rangle = \frac{(1+\gamma)U_i}{2\omega T_s} [sin(\omega t - \delta)]_0^{T_s} \tag{4}$$

Considering the available observations, we obtain a determined value of $u_m = 0.40$ m s^{-1} and we can estimate a value for c for the two-layer water column, by applying the equations (Gerkema and Zimmerman, 2008):

$$c = c_0 \left(1 + \frac{h_2 - h_1}{2h_1 h_2} a\right); c_0 = \sqrt{g \frac{(\rho_2 - \rho_1)}{\rho_2} \frac{h_1 h_2}{h_1 + h_2}} \tag{5}$$

where c_0 is the linear phase speed; h_i and ρ_i the thicknesses and densities; g is the gravitational acceleration, and a is the soliton amplitude. Using representative mean values $\rho_1 = 1027.00$ kg m^{-3}, $\rho_2 = 1028.00$ kg m^{-3}, and $a = 50$ m for the two transits and the thicknesses $h_1 = 100$ m and $h_2 = 500$ m for the transit CS – ER, and $h_1 = 100$ m and $h_2 = 700$ m, for the transit T - E, which are based on different data sources (Bray et al., 1995; MEDAR Group, 2002; Vázquez et al., 2008), mean values $c = 1.07$ m s^{-1} and $c = 1.11$ m s^{-1} are obtained for CS - ER and T - E transits, respectively. Substituting these values, u_m and c, into Eq. (2), theoretical values of T_s for a given tidal current amplitude of the starting point, U_i, may be calculated by imposing the condition $c_m = L/T_s$; L being the distance between the two considered points. We applied these computations to the transits between T and E and between CS and ER using the remaining parameter values shown in Table 2. In the same table the resulting travel times (T_s), mean current value u_m and characteristic amplitude of subinertial variability Δu_m (m s^{-1}) are shown. These are based on historical records over CS and observations from HFR. These variations are introduced to assess the contribution of the subinertial variation, and its magnitude has been deduced from the observed subinertial current variability shown in Figs. 3 and 4 for the May 2003 period, and in Fig. 12 for the September-October 2015 period.

The computed T_s using a soliton amplitude of $a = 50$ m and 100 m (Table 2) are also represented in Fig. 13 to compare the distribution of these theoretical values with the observed ones. As can be seen, the variation range of the observed T_s is overall contemplated by the predicted values based on Eq. (2). This result indicates that although the T_s variability is related to the intensity of the eastward current following the soliton release, a significant part of the remaining variability could be explained by the subinertial variation of the upper layer current. Taking into account that the Maximum Eastward Current (MEWC) coincides with solitons of higher amplitude, which will move faster than predicted by Eq. (5), the contribution of these changes in the speed to the net travel times for each of the analysed transits must be assessed. To do so, we computed the T_s values, for the case of MEWC = 2.5 m s^{-1}, corresponding to a soliton amplitude of $a = 100$ m, representative of the largest solitons generated during spring tides. The resulting values are shown in Table 2 in bold numbers and between parentheses, and they are representative of the largest amplitude events, which are more likely to occur in spring tide periods coinciding with greater tidal current maximums. Subsequently, we defined the range of variability caused by the MEWC changes as the difference between the T_s values corresponding to MEWC = 0.6 m s^{-1} and MEWC = 2.5 m s^{-1}. Analogously, we define the range of variability caused by the soliton speed changes related to increased amplitude, as the difference between the first of the previous T_s values and the value given in bold numbers. In Table 2 these ranges are 1.37 h and 2.28 h for the transit T-E and 1.22 h and 1.54 h for the transit CS - ER. From these numbers, an appreciable increase in the

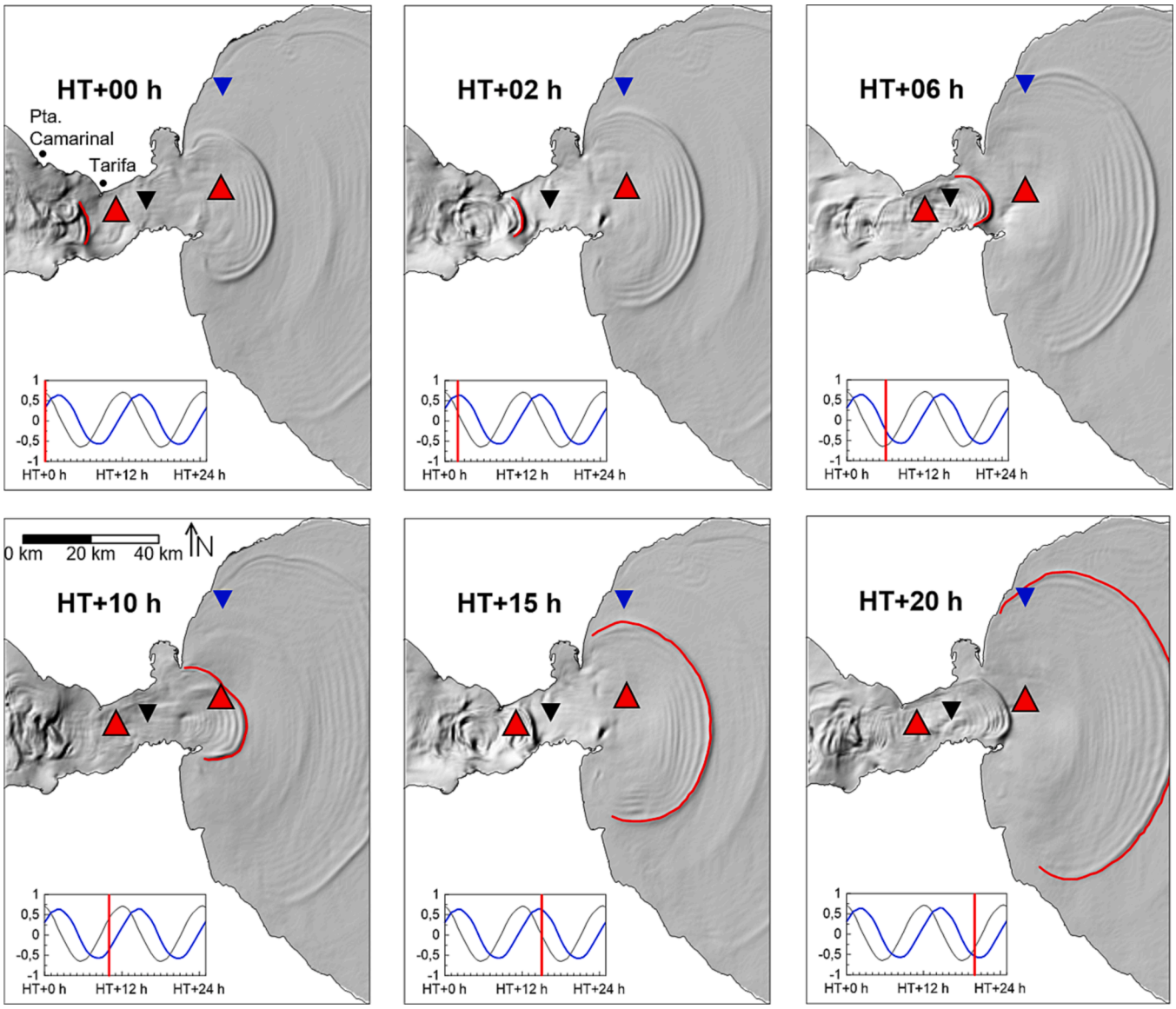

Fig. 11. Simulations from the UCA3D model of the Sea Surface Height (SSH) induced by the internal solitons generated around Camarinal Sill (CS). The first SSH front coloured in red is used to track the internal solitons propagation from CS to the thermistors mooring (TH) (inverted blue triangle). The time in hours relative to the first map is indicated. Embedding small plots show the time series of tidal elevation (black line, m) and barotropic tidal current (blue line, m s^{-1}) over CS with indication through the vertical red line of the time location of each map. Red triangles depict the position of moorings in T (Tarifa) and E (east of the Strait of Gibraltar), and black inverted triangles indicate the position of ER point (Eastern Radar) (Fig. 1a). HT: High Tide. (For interpretation of the references to color in this figure legend, the reader is referred to the web version of this article.)

T_s range (2.28 / 1.37) is expected in the transit T - E while a less important change (1.54 / 1.22) is expected in the transit CS - ER. Therefore, we conclude that a significant contribution to the travel times from the spring-neap variation of the soliton propagation speed cannot be discarded, at least for the transit T - E.

In the May 2003 period, we found a greater scattering of the travel time values around their mean theoretical estimates (those corresponding to $\Delta u_m = 0$) for small and moderate eastward current maxima (0.50–1.50), which could be related to the coincidence in the occurrence of these values with the eastward and westward intensification of the subinertial currents. Furthermore, most of the higher eastward current maxima occur during the westward intensification of the subinertial current and this could explain the gathering of the corresponding travel times below the mean values.

However, during the September - October 2015 period, this scattering in travel time values is found throughout the whole range of eastward current maxima, which may be related to the continuous alternation of eastward and westward intensification of subinertial current in coincidence with both small and high values of eastward current maxima.

4.2. Propagation speed of internal solitons in the transit from ER to TH

To interpret the observed variability of soliton travel times we estimated the propagation speed of solitons in their transit from ER to TH. These estimations are based on the TH record by previously inferring there the density profiles in the aforementioned record from the temperature profiles recorded by the thermistors chain. With this aim, a linear regression analysis was performed based on the available salinity and temperature profiles (CTD measurements, Table S1) closest to the mooring site (green and orange dots in Fig. 1b-c). It was carried out to use the resulting linear function related to salinity and temperature to infer the salinity profiles corresponding to the mooring site. Moreover, the corresponding density profiles that characterize the stratification

Table 2
Theoretical mean travel times of solitons computed by Eq. (2), for the two considered transits. U_i: tidal current amplitude; u_m: mean current value; Δu_m: characteristic amplitude of subinertial variability; c: mean soliton propagation, computed using Eq. (2); γ is a constant in the linear variation of tidal current amplitude; L (m) is the distance between considered points, and δ (°) is an adjustment for the tidal current phase. MEWC: predicted Maximum Eastward Current; T: Tarifa mooring; E: east of the Strait mooring, and ER: Eastern Radar (see map of Fig. 1a). The T_s (hours) values have been computed using a soliton amplitude of $a = 50$ m as a representative mean value. Results corresponding to $a = 100$ m, for the case of MEWC = 2.5 m s^{-1} are also shown in parenthesis and bold letters.

TRANSITS	MEWC at CS (m s^{-1})	U_i (m s^{-1})	γ	L (m)	δ (°)	T_s (h) u_m (m s^{-1})	T_s (h) u_m - Δu_m (m s^{-1})	T_s (h) $u_m + \Delta u_m$ (m s^{-1})
T → E (May 2003) $u_m = 0.40$ (m s^{-1}) $\Delta u_m = 0.30$ (m s^{-1})	0.60	0.30	0.28	36,000	30	7.00	8.26	6.06
	1.00	0.70				6.82	8.26	5.83
	1.50	1.30				6.54	8.26	5.49
	2.00	1.70				6.15	8.25	5.10
	2.50	2.30				5.63 **(4.72)**	8.24	4.69
CS → ER (Sep - Oct 2015) $u_m = 0.30$ (m s^{-1}) $\Delta u_m = 0.20$ (m s^{-1})	0.60	0.24	0.17	35,000	135	6.27	7.80	5.29
	1.00	0.56				5.90	7.16	5.07
	1.50	1.04				5.54	6.51	4.86
	2.00	1.70				5.26	6.04	4.69
	2.50	1.84				5.05 **(4.73)**	5.69	4.55

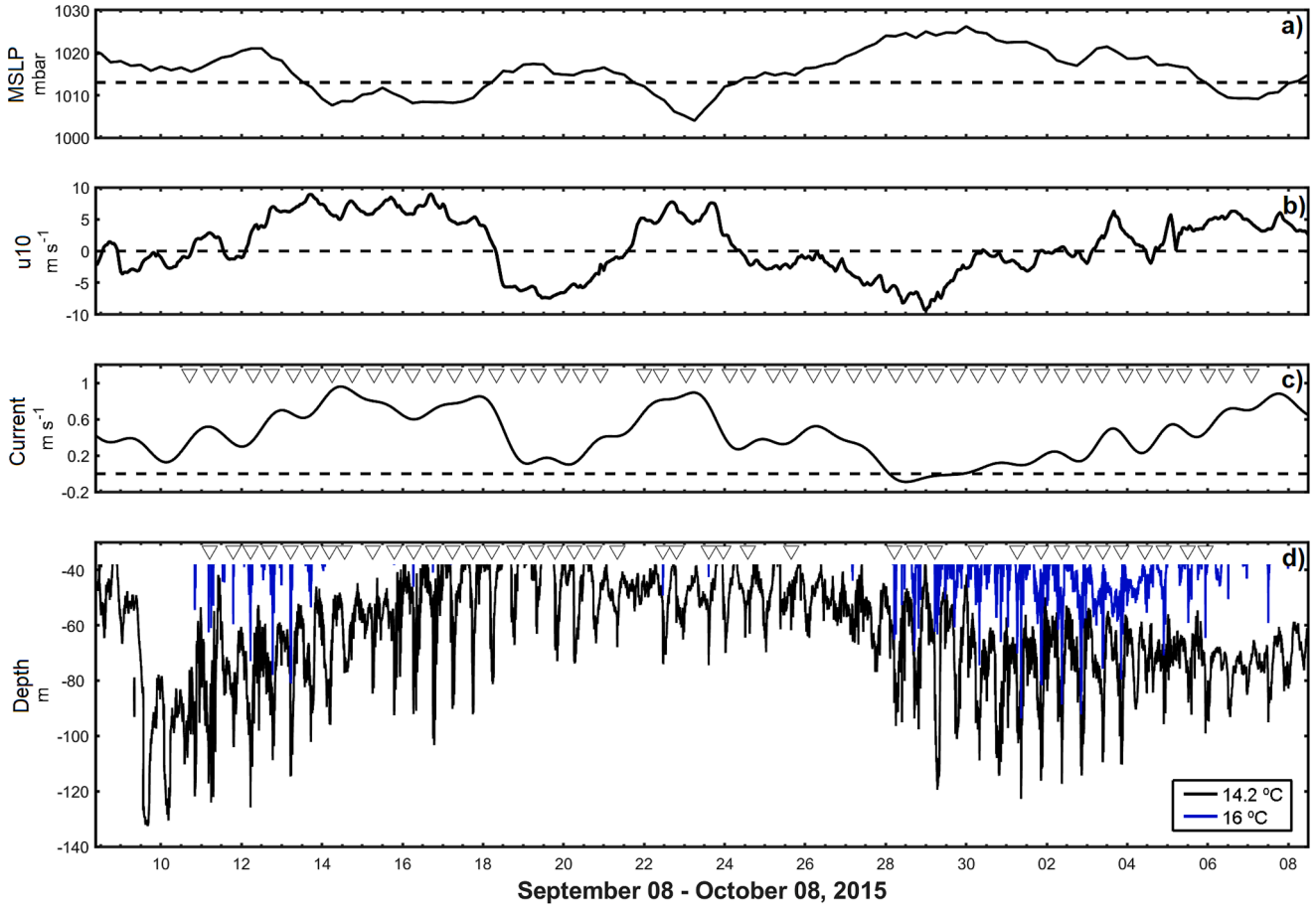

Fig. 12. (a) Variability of the Mean Sea Level Pressure (MSLP, mbar) over the western Mediterranean. The horizontal black dotted line delimits the high (>1013 mbar) and low (<1013) pressure; (b) zonal component of wind at 10 m height (m s^{-1}) over the Alboran Sea.; (c) subinertial zonal component of the current (m s^{-1}) across the Strait of Gibraltar (vertical black transect in Fig. 1b). The horizontal black dashed line in (b) delimits the zero reference which indicates the zonal wind directed to east/west when it is higher/lower than 0 m s^{-1}, and in (c) delimits the zero reference which indicates the flow directed to the east/west when it is higher/lower than 0 m s^{-1}. White inverted triangles denote the dates when internal solitons reach the Eastern Radar point (ER in Fig. 1a). (d) Vertical variability of the depth position of the 16 °C (blue line) and 14.20 °C (black line) isotherms. White inverted triangles denote the dates when internal solitons reach the mooring. Information about the times is detailed in the supplementary material (Table S4). (For interpretation of the references to color in this figure legend, the reader is referred to the web version of this article.)

conditions there were assessed from the linear function. Similar experiences of density profile reconstruction have been applied by other authors (Reseghetti, 2007; Goes et al., 2018). The linear regression analysis yielded a significant correlation ($p < 0.001$) with $R^2 = 0.88$. The relation between the salinity (S) and the temperature (T, °C) is given using S = -0.57 * T + 45.71, which allows us to predict the temporal evolution of the salinity from the temperature records acquired by the thermistors chain. Subsequently, the temporal evolution of the seawater

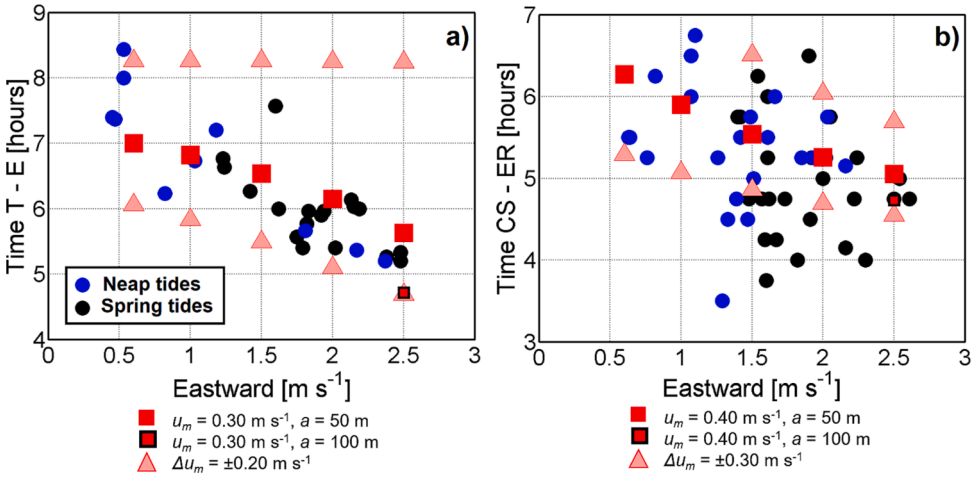

Fig. 13. Relation between the maximum eastward current intensity (m s^{-1}) reached over Camarinal Sill (CS, tidal current prediction at 45 m depth) and the travel time of the solitons when they reach both Tarifa and the east of the Strait moorings (T and E, respectively) and ER positions (see locations in Fig. 1a) for the 2003 period (a) and for the 2015 period (b). u_m: predicted travel times of solitons using Eq. (2); Δu_m: predicted travel times of solitons from a mean current modified; a: amplitude of the soliton (m). The y-axis indicates travel times (hours) and the x-axis eastward current intensity (m s^{-1}).

density at the TH site was computed using the standard state equation for seawater (TEOS-10). It was computed from both temperature and the estimated salinity.

Once the density profiles were calculated at the TH site, two different approaches to compute the soliton propagation speed were used. The first one is based on Eq. (5) for a two-layer water column, Atlantic and Mediterranean layers, separated by an interface (AMI). This approach has been used extensively in the Strait of Gibraltar (Izquierdo et al., 2001; Ramírez-Romero et al., 2012), and even in the western Alboran Sea (Gascard and Richez, 1985). Based on the analysis presented in section 3.2, the interface depth is assumed to be at the depth of the 37.30 isohaline. The corresponding ρ_1 and ρ_2 values are obtained by averaging the density profile at each layer above and below this isohaline.

The second approach is more realistic considering a continuously stratified water column specified by the available density profiles. In this case, the phase speed of a first-mode internal solitary wave is computed as (Lee and Beardsley, 1974):

$$c = c_0 + \alpha a \tag{6}$$

where a (m) is the amplitude of the solitary wave, α is the nonlinear coefficient (s^{-1}); and c_0 (m s^{-1}) is the linear phase speed of the first baroclinic mode, which is equal to the highest eigenvalue of the Sturm-Liouville problem (Lee and Beardsley, 1974; Vlasenko et al., 2005).

$$\frac{c_0^2}{N^2(z)}\overline{\Psi}_{zz}(z) = \overline{\Psi}(z) \tag{7}$$

$\overline{\Psi}(z)$ is a dimensionless function (first baroclinic mode) that determines the vertical structure of the stream function amplitude corresponding to the 2D problem and disregarding Earth rotation effects. Vertical coordinate z (depth) is oriented upwards, and $N(z)$ is the buoyancy frequency profile characterizing the background stratification. Subscripts indicate derivatives concerning the z coordinate. The parameter α is determined as (Liu, 1988):

$$\alpha = -\frac{c_0}{2}\frac{\int_0^H \overline{\Psi}_z^3(z)dz}{\int_0^H \overline{\Psi}_z^2(z)dz} \tag{8}$$

where H (m) is the bottom depth. Function $\overline{\Psi}(z)$ inside Eq. (8) must be previously normalized concerning its maximum value.

As the TH observations only spanned the depth range between 38 and 140 m, over a bottom depth of 150 m, the density profiles needed to

Table 3
Propagation speed (m s^{-1}) at different points (isobaths from 700 to 150 m depth) along a transect from the easternmost Strait of Gibraltar (black dots in Fig. 1b) and the thermistor mooring location (TH) during different time intervals (spring and neap tides) by the time that the thermistor chain was moored. The speed has been calculated using both methodologies described in the text: (i) two-layer approximation, and (ii) continuously stratified fluid. Minimal and maximal amplitude (a) of 15 and 50 m were considered in these results.

Two-layer approximation	700 m	600 m	500 m	400 m	300 m	200 m	TH 150 m
SPRING 1 10–16 September	1.13 ± 0.17	1.10 ± 0.12	1.07 ± 0.12	1.03 ± 0.11	0.96 ± 0.93	0.84 ± 0.70	0.72 ± 0.04
NEAP 1 19–25 September	0.98 ± 0.17	0.95 ± 1.49	0.92 ± 0.14	0.87 ± 0.13	0.85 ± 0.12	0.74 ± 0.10	0.67 ± 0.08
SPRING 2 25–30 September	1.36 ± 0.16	1.31 ± 0.15	1.25 ± 0.14	1.17 ± 0.13	1.08 ± 0.11	0.94 ± 0.08	0.81 ± 0.05
NEAP 2 01–08 October	1.55 ± 0.15	1.52 ± 0.15	1.48 ± 0.14	1.43 ± 0.13	1.34 ± 0.11	1.17 ± 0.07	1.00 ± 0.03
Continuously stratified fluid	**700 m**	**600 m**	**500 m**	**400 m**	**300 m**	**200 m**	**TH 150 m**
SPRING 1 10–16 September	1.01 ± 0.08	0.99 ± 0.08	0.97 ± 0.08	0.93 ± 0.08	0.87 ± 0.08	0.76 ± 0.06	0.66 ± 0.05
NEAP 1 19–25 September	0.89 ± 0.02	0.83 ± 0.03	0.79 ± 0.05	0.76 ± 0.07	0.72 ± 0.07	0.64 ± 0.06	0.57 ± 0.05
SPRING 2 25–30 September	1.26 ± 0.02	1.11 ± 0.03	1.08 ± 0.05	1.02 ± 0.08	0.96 ± 0.09	0.86 ± 0.09	0.76 ± 0.07
NEAP 2 01–08 October	1.41 ± 0.15	1.39 ± 0.15	1.36 ± 0.15	1.34 ± 0.15	1.37 ± 0.05	1.15 ± 0.13	1.04 ± 0.11

solve Eq. (7) were extrapolated from surface to bottom by assuming a constant value out of the TH depth range.

Table 3 compares the resulting average propagation speeds estimated using both approaches for the different neap and spring tides presented within the TH mooring record. Note that this propagation speed has been computed for different locations between the eastern mouth of the Strait and the TH mooring (black dots in Fig. 1b). For all these additional locations, the upper-layer thickness and upper- and lower-layer densities are assumed to be the same as those found in the TH mooring.

Differences in the computed speeds between the two different approaches (two-layer approximation and continuously stratified column) are small, but speeds are consistently slightly larger for the two-layer approach. In addition, the speeds corresponding with the first half of the record (from September ~ 10 to 25) are lower than those of the second half (from September 25 to the end) with no clear variation pattern between spring and neap tides. The soliton speed during the second half increased by approximately 38 % on average compared to the first half.

4.3. Variability of the observed soliton travel times and comparison with the theoretical travel time deduced from the soliton propagation speed computations

In Table 4, average values of c are shown for the continuous stratification case, along the transit between the eastern Strait mouth, through the above-mentioned black dots indicated in the map of Fig. 1b. Considering a mean bottom depth along the transit from the eastern mouth to the TH of 450 m and a constant value of $\rho_2 = 1028.50$ kg m^{-3}, a change in the upper layer thickness (h_1) from 30 m to 80 m provokes changes in c of 0.08 and 0.10 m s^{-1} for upper layer densities (ρ_1) of 1027.50 and 1027.00 kg m^{-3}, respectively. However, a change in ρ_1 from 1027.50 to 1027.00 kg m^{-3} provokes a change in c of 0.19 and 0.20 m s^{-1} for h_1 values of 30 and 80 m, respectively. From these numbers, it is clear that the greater changes in c values are the result of changes in the upper layer density. The mean upper layer density corresponding to the different periods is also shown. As expected, the two last periods present a greater ρ_1, by the resulting c values: the greater ρ_1, the greater c.

In the same table (Table 4) the observed soliton travel time (OT_s) can be found together with those predicted by using the c computations (PT_s). As a general rule, we found that for all the studied periods OT_s, values are greater than PT_s ones, but this difference increased significantly for the last two periods. In light of these comparisons, it is clear that the changes in c values caused by the changes in stratification throughout the different periods cannot explain the variability exhibited by the OT_s values. Therefore, another mechanism should explain this difference between observed (OT_s) and predicted (PT_s) results. This mechanism is addressed in the next section.

Table 4
Spatially averaged densities (ρ, kg m^{-3}) (in the upper and lower layer) and propagation speed of solitons (c, m s^{-1}) along the locations indicated by the black circles in the map of Fig. 1b. The observed mean travel times are also shown (OT_s) and the predicted travel times (PT_s) using the corresponding c values for the four periods considered.

Time Period	ρ_1 (kg m^{-3})	ρ_2 (kg m^{-3})	c (m s^{-1})	Observed OT_s (h)	Predicted PT_s (h)
SPRING 1 (10–16 Sep)	1027.28	1028.53	0.93	10.93	7.93
NEAP 1 (19–25 Sep)	1027.59	1028.58	0.76	10.27	9.69
SPRING 2 (25–30 Sep)	1026.99	1028.53	1.02	11.36	7.23
NEAP 2 (1–8 Oct)	1026.03	1028.52	1.34	12.13	5.51

5. Discussion

5.1. Temporal variability of internal solitons

The presence of soliton trains in the western Alboran Sea has been identified using different satellite products (e.g., SAR, HICO – Hyperspectral Imager for the Coastal Ocean) in several studies (e.g., Navarro et al., 2018; Dessert et al., 2022) or numerical simulations (e.g., Álvarez et al., 2019). Nevertheless, there are very few studies that use in-situ methodologies with adequate temporal sampling rates beyond the eastern mouth of the Strait, for example, Pistek and La Violette (1999); Sánchez-Garrido et al. (2008) or recently Dessert et al. (2022).

The most likely generation place of those solitons is widely accepted to be CS in the Strait of Gibraltar, where large amplitude internal waves are generated on its lee side during the westward phase of the tidal current when the current is intense enough. Vázquez et al. (2008) reported that these internal waves were generated when the maximum intensity of the westward tidal current at 45 m depth over CS was equal to or>1 m s^{-1}. They also found that the internal waves were released once the westward tidal current weakened to 0.60 m s^{-1}. In our analysis, the generation of large amplitude internal waves was produced during each westward phase of tidal current over CS, although during the neap tide events, the internal solitons were usually of lesser amplitudes. Internal wave generation events took place even when the predicted maximum westward tidal current intensity (at 45 m depth) over CS was<1 m s^{-1} but the internal Froude number G^2 reached values greater than one.

To estimate the travel time of internal solitons through the different stages of their journey toward the TH mooring, we used the time at which the internal waves were released from CS as a reference. That is when predicted G^2 over CS has a value lower than 1. Using this reference time, the analysis of the data recorded in the mooring T (Tarifa in Fig. 1a) during 2003 has allowed us to estimate the travel time of the soliton on its journey from CS to T, which lies mainly within the range of 3 – 5 h. These times did not show any correlation with the intensity of maximum the eastward tidal current (Fig. 3). It must be noted that independently of the intensity of these maximums, the release took place when the westward current intensity slows down at a certain value (i.e., 0.60 m s^{-1}), consequently the travel time of solitons are similar. During this initial transit (CS-T), solitons arrive at the T mooring with a considerable time lapse before the maximum eastward tidal current is reached at T mooring (as shown in Fig. 5). Therefore, solitons barely feel the advection effect of the stronger eastward current occurring during spring tides.

In addition, using the simultaneous records of the moorings at Tarifa (T) and the east of the Strait of Gibraltar (E) (Fig. 1a), it was possible to estimate the travel time between both locations. They are dependent on the maximum intensity of eastward tidal currents, a characteristic already identified by Sánchez-Garrido et al. (2008) based on the same data set. In this case, the estimated travel time was situated in the range of 5 – 8 h and showed a clear spring-neap variability, which is due to the greater values of the maximum eastward tidal current during spring tides compared to neap tides (Fig. 4). For the September - October 2015 period, similar results were found for the transit between CS and ER (Eastern Radar) sites. Here, the estimated travel time falls within the range of 4 – 7 h, showing a clear spring/neap variability as well. Nonetheless, the relationship between soliton travel times and maximum eastward current seems to be modulated by the effects of the subinertial variability in the upper layer current. This subinertial current contribution may induce variations in the travel times of ca. 2 h (Table S4).

To estimate the travel time of the solitons in the last stage of their journey from the eastern mouth of the Strait to the TH mooring, we computed the propagation speed of solitons as a function of the temperature-synthesized density profiles from the thermistor-chain records. These calculations were done for profiles averaged throughout

the different spring and neap tide periods and no evidence of fortnightly variability was found in the computed propagation speeds. The different stratification conditions found in these spring and neap tide periods yielded a range of variation of the propagation speeds between 0.76 and 1.34 m s^{-1}, which involves travel time differences of ca. 4 h. However, the travel times resulting from these propagation speed estimates are less than the observed ones during the second half of the analysis period.

Considering the rather permanent presence of the Coastal Cyclonic Gyre (CsCG) in the NW Alboran Sea (Figure S2), the western branch of this gyre flowing close to the coast should affect, to some extent, the propagation of the lateral portion of solitons fronts closer to the coast. These larger travel times seem to be related to a wider descending branch of the CsCG which encompasses the TH mooring site slowing down the propagation speed of solitons before they reach the mooring. During easterlies, the CsCG is detached from the coast (Sarhan et al., 2000) due to the presence of a coastal countercurrent directed towards the Strait of Gibraltar (Bolado-Penagos et al., 2021). The travel time for the whole journey (from CS to TH) varies between 14 and 20 h (for spring and neap tides, respectively).

As can be seen in Fig. 7, an apparent fortnightly cycle is indeed presented in both the number of soliton arrivals and the soliton amplitudes. Therefore, during spring tides the number of large-amplitude soliton arrivals is higher, and solitons show greater amplitude than during neap tides. It is worth noting that during the studied neap tide periods a significant diurnal inequality was presented by the tidal current prediction over CS. This fact, along with the additional contribution of subinertial flow that favours the westward current intensities, could mean that some westward tidal current maximum reach intensities close to 1 m s^{-1} at a diurnal frequency.

Despite these sources of variability, the described results seem to support that the recorded internal soliton signals over the continental shelf/slope in the NW sector of the Alboran Sea (TH mooring) are, as expected, those arising from the large amplitude internal waves generated on the lee side of CS in the Strait of Gibraltar during the westward phase of tidal current: the so-called A-Waves (Watson and Robinson, 1990). Nonetheless, the arrival of another type of wave, such as the O-Waves or other local sources, cannot be discarded. The isolated identification of these two types of solitons (A- and O-Waves) is very difficult since they coincide over the eastern mouth of the Strait with time, as shown by the observations reported in Watson and Robinson (1990) and the UCA3D model simulations presented in section 3.3 (Fig. 9).

5.2. *Biological implications of the effect of subinertial variability on the soliton arrivals on the continental slope of the NW-Alboran Sea coast*

As observed from the temporal evolution of the vertical temperature profiles recorded at the TH mooring (Fig. 7e) solitons regularly reach the Alboran continental slope during both spring and neap tides. Nevertheless, the spring tide events are shown to be of greater amplitude.

Fig. 14 shows the results obtained with an undulating CTD along a transect perpendicular to the coast close to the TH mooring position (red line in Fig. 1b). The undulating CTD was moored at a depth of between 30 and 60 m (Fig. 14a) and it recorded internal solitons (Fig. 14b) progressing over the slope and continental shelf (from 200 to ~ 50 m depth, Fig. 14c). This event was already analysed by Vázquez et al. (2009) and Dessert et al. (2022). The ASAR image (Fig. 14d) was acquired the same day as the CTD observations (on October 1, 2008, at 10:00 UTC), and shows the arrival of internal solitons at the northwestern coast of the Alboran Sea. Before reaching the continental shelf, they are depression solitons or waves out of the shelf, but they are transformed into elevation solitons or waves once they are over the shelf (Fig. 14b). However, they are transformed into elevation solitons once they progress over the shelf. The unavoidable fate of the aforementioned elevation waves is their breaking and the production of subsequent vertical mixing on the water column over the shelf. This breaking is likely to occur when the bottom depth approaches the upper layer thickness (Lamb, 2003; Miramontes et al., 2020). The vertical mixing processes associated with these breaking events could be able to supply upwelled colder and nutrient-enriched water to this coastal region (Villamaña et al., 2017) contributing to the upwelling characteristics of the area (Sarhan et al., 2000) where the CsCG is usually emplaced. Moreover, this cyclonic gyre is an area with a great capacity to retain the phytoplankton and nutrients for long periods, allowing long residence times of the phytoplankton populations (Bolado-Penagos et al., 2020). Fig. 14b shows the asymmetry in the soliton (as observed in Fig. 6). This asymmetry could also cause changes in the vertical heat transport and nutrient concentrations as observed in other studies (Dong et al., 2015; Chen et al., 2019).

In addition, considering that soliton displacement is mainly channelized by the location of the averaged depth of the AMI, a shallower (deeper) AMI may favour solitons breaking in shallower (deeper) bottom depths, conditioning the shoreward reaching of the vertical mixing exchange produced by the solitons breaking. However, it is reasonable to think that the shallower the breaking the greater the phytoplankton response to the produced nutrient inputs since these would be closer to

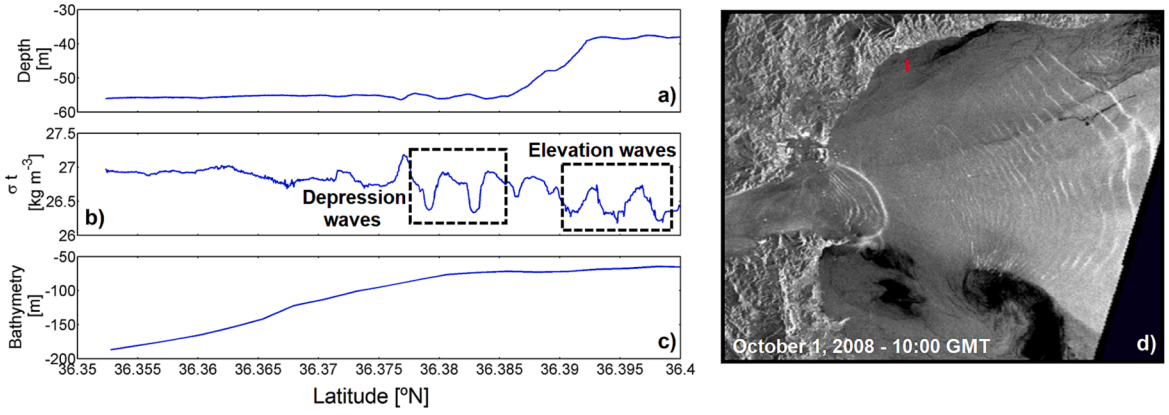

Fig. 14. Profiles of different variables recorded along the transect indicated in Fig. 1b (vertical red line) northeast of thermistors (TH) mooring. (a) Depth (m) position of the undulating Conductivity Temperature and Depth (CTD). (b) Density (kg m^{-3}) recorded at that depth. Dotted rectangles indicate the transformation of the recorded solitons while they progress over the continental shelf. (c) Bathymetry (m) along the studied section. (d) Internal wave trains entering the Alboran Sea from the Strait of Gibraltar as captured by the ASAR (Advanced Synthetic Aperture Radar) sensor of the ENVISAT satellite at 10:00 UTC on October 1, 2008. The vertical red line shows the location of the transect. (For interpretation of the references to color in this figure legend, the reader is referred to the web version of this article.)

the euphotic zone.

As mentioned, in conditions of intense and persistent easterly winds, the CsCG and the phytoplankton populations inside it are displaced southeastward. This provokes the deepening of the AMI in the continental slope area, moving the breaking of solitons away from the Spanish coast, meaning they could break in other areas (e.g., the African coast). The latter situation, along with the low phytoplankton concentration, would render the phytoplankton growth in the studied area very difficult. Under westerly wind conditions, the CsCG is located near the coast occupying the NW corner of the Alboran Sea. This situation matches a shallow AMI, which favours soliton breaking closer to the continental shelf and hence supplying nutrients within the euphotic zone.

These ideas encourage further assessment of the presence of the internal solitons and the role of the soliton breaking in sustaining the nutrient supply to this coastal area.

6. Conclusions

In this study, we have analysed the presence of internal solitons within the Strait of Gibraltar and the Alboran Sea from different datasets and numerical modelling. The recorded internal soliton signals over the continental shelf/slope in the NW sections of the Alboran Sea (TH mooring) seem to be, as expected, arising from the large internal waves generated on the lee side of CS in the Strait of Gibraltar during the westward phase of the tidal current.

The time sequence of the soliton arrivals over the continental slope in the NW Alboran Sea shows a clear fortnightly cycle in both the regularity of soliton arrivals and soliton amplitudes. During spring tides, the regularity of soliton arrivals is higher and solitons show greater amplitude than during neap tides. During neap tides, a significant diurnal inequality is presented in the tidal current prediction over CS.

The observed arrival times of the solitons at the TH mooring oscillate between 14, during spring tides, and 20 h, during neap tides. There is also a clear fortnightly variability of travel times, which is mainly a result of the greater values of the maximum eastward tidal current during spring tides. However, to fully explain the observed variability of these travel times, the atmospherically-forced subinertial variability that affects both the flow through the Strait of Gibraltar and the mesoscale structures of the Alboran Sea, must be taken into account.

Declaration of Competing Interest

The authors declare that they have no known competing financial interests or personal relationships that could have appeared to influence the work reported in this paper.

Data availability

Data will be made available on request.

Acknowledgments

The authors gratefully acknowledge the crew and technical staff (*Unidad de Tecnología Marina*, UTM) of the R.V. *Sarmiento de Gamboa* for their help during the MEGAN cruise and the scientific team of the MEGAN project. The authors also acknowledge the Spanish *Puertos del Estado* for the freely available HFR dataset obtained from their website. The authors also thank NASA for providing access to MODIS-Aqua for the daily L3 images of Chl-*a*. Atmospheric forcing data were downloaded from ERA5 hourly data on single levels from 1940 to the present in the context of the Copernicus Climate Change Service (C3S). This study has been supported by the Spanish National Research Plan through the MEGAN project: CTM2013-49048, and by the European Union's Interreg VA España – Portugal (POCTEP) 2014-2020 project OCASO (0223_OCASO_5_E). Marina Bolado-Penagos and Iria Sala were supported by a grant from the FPI fellowship program. Marina Bolado-Penagos carried out a short stay at the Department of Ocean Systems (NIOZ; Texel, the Netherlands) that was supported by a grant from the FPI fellowship program (EEBB-I-18-12889). The authors would like to express great appreciation to the anonymous reviewers for their valuable comments which helped to improve the manuscript

Appendix A. Supplementary material

Supplementary data to this article can be found online at https://doi.org/10.1016/j.pocean.2023.103077.

References

Álvarez, Ó., González, C.J., Mañanes, R., López, L., Bruno, M., Izquierdo, A., Gómez-Enri, J., Forero, M., 2011. Analysis of short-period internal waves using wave-induced surface displacement: A three-dimensional model approach in Algeciras Bay and the Strait of Gibraltar. J. Geophys. Res. 116, C12033. https://doi.org/10.1029/2011JC007393.

Álvarez, Ó., Izquierdo, A., González, C.J., Bruno, M., Mañanes, R., 2019. Some considerations about non-hydrostatic vs. hydrostatic simulation of short-period internal waves. A case study: The Strait of Gibraltar. Cont. Shelf Res. 181, 174–186. https://doi.org/10.1016/J.CSR.2019.05.016.

Apel, J.R., 2000. Oceanic internal waves and solitons. An atlas of oceanic internal solitary waves. Global Ocean Associates. Prepared for Office of Naval Research - Code 322PO, 1–40.

Apel, J.R., Worcester, P.F., 2000. Internal solitons near Gibraltar: A longitudinal study using ERS-1 & 2 SAR imagery, in: ERS–Envisat Symposium: Looking Down to Earth in the New Millennium, European Space Agency, ESRIN/Publications. pp. 7–16.

Armi, L., Farmer, D.M., 1985. The internal hydraulics of the Strait of Gibraltar and associated sills and narrows. Oceanol. Acta 8, 37–46.

Armi, L., Farmer, D., 1988. The flow of Mediterranean water through the Strait of Gibraltar. Prog. Oceanogr. 21, 41–82.

Bartual, A., Macías, D., Gutierrez-Rodriguez, A., García, C.M., Echevarría, F., 2011. Transient pulses of primary production generated by undulatory processes in the western sector of the Strait of Gibraltar. J. Mar. Syst. 87, 25–36. https://doi.org/10.1016/j.jmarsys.2011.02.021.

Bolado-Penagos, M., González, C.J., Chioua, J., Sala, I., Gomiz-Pascual, J.J., Vázquez, Á., Bruno, M., 2020. Submesoscale processes in the coastal margins of the Strait of Gibraltar. The Trafalgar – Alboran connection. Prog. Oceanogr. 181, 102219 https://doi.org/10.1016/j.pocean.2019.102219.

Bolado-Penagos, M., Sala, I., Gomiz-Pascual, J.J., Romero-Cózar, J., González-Fernández, D., Reyes-Pérez, J., Vázquez, A., Bruno, M., 2021. Revising the Effects of Local and Remote Atmospheric Forcing on the Atlantic Jet and Western Alboran Gyre Dynamics. J. Geophys. Res. Oceans 126. https://doi.org/10.1029/2020JC016173.

Brandt, P., Alpers, W., Backhaus, J.O., 1996. Study of the generation and propagation of internal waves in the Strait of Gibraltar using a numerical model and synthetic aperture radar images of the European ERS 1 satellite. J. Geophys. Res. C: Oceans 101, 14237–14252. https://doi.org/10.1029/96JC00540.

Bray, N.A., Ochoa, J., Kinder, T.H., 1995. The role of the interface in exchange through the Strait of Gibraltar. Journal of Geophysical Research 100, 10.755-10.776.

Bruno, M., Juan Alonso, J., Cózar, A., Vidal, J., Ruiz-Cañavate, A., Echevarría, F., Ruiz, J., 2002. The boiling-water phenomena at Camarinal Sill, the strait of Gibraltar. Deep Sea Res. Part II 49, 4097–4113. https://doi.org/10.1016/S0967-0645(02)00144-3.

Candela, J., Winant, C.D., Bryden, L., 1989. Meteorologically forced subinertial flows through the Strait of Gibraltar. J. Geophys. Res. 94, 12667–12679.

Chen, L., Zheng, Q., Xiong, X., Yuan, Y., Xie, H., Guo, Y., Yu, L., Yun, S., 2019. Dynamic and Statistical Features of Internal Solitary Waves on the Continental Slope in the Northern South China Sea Derived From Mooring Observations. J. Geophys. Res. Oceans 124, 4078–4097. https://doi.org/10.1029/2018JC014843.

Chioua, J., Bruno, M., Vázquez, A., Reyes, M., Gomiz, J.J., Mañanes, R., Álvarez, O., González, C., López, L., Gómez-Enri, J., 2013. Internal waves in the Strait of Gibraltar and their role in the vertical mixing processes within the Bay of Algeciras. Estuar. Coast. Shelf Sci. 126, 70–86. https://doi.org/10.1016/j.ecss.2013.04.010.

Criado-Aldeanueva, F., Soto-Navarro, F.J., García-Lafuente, J., 2012. Seasonal and interannual variability of surface heat and freshwater fluxes in the Mediterranean Sea: Budgets and exchange through the Strait of Gibraltar. Int. J. Climatol. 32, 286–302. https://doi.org/10.1002/joc.2268.

Dessert, M., Honnorat, M., Le Caillec, J.-M., Messager, C., Carton, X., 2022. Estimating the Pycnocline Depth From the SAR Signature of Internal Waves in the Alboran Sea. IEEE J. Sel. Top. Appl. Earth Obs. Remote Sens. 15, 9048–9061. https://doi.org/10.1109/JSTARS.2022.3214298.

Dong, J., Zhao, W., Chen, H., Meng, Z., Shi, X., Tian, J., 2015. Asymmetry of internal waves and its effects on the ecological environment observed in the northern South China Sea. Deep Sea Res. Part I 98, 94–101. https://doi.org/10.1016/j.dsr.2015.01.003.

Echevarría, F., García-Lafuente, J., Bruno, M., Gorsky, G., González, N., García, C.M., Gómez, F., Vargas, J.M., Picheral, M., Striby, L., Varela, M., Alonso, J.J., Reul, A., Cózar, A., Prieto, L., Sarhan, T., Plaza, F., Jiménez-Gómez, F., 2002. Physical – biological coupling in the Strait of Gibraltar. Deep Sea Res., Part II 49, 4115–4130.

García-Lafuente, J., Álvarez-Fanjul, E., Vargas, J.M., Ratsimandresey, W., 2002b. Subinertial variability in the flow through the Strait of Gibraltar. Journal of Geophysical Research 107 (C10), 3168, doi:10.1029/2001JC001104.
García-Lafuente, J., Delgado, J., Vargas, J.M., Vargas, M., Plaza, F., Sarhan, T., 2002a. Low-frequency variability of the exchanged flows through the Strait of Gibraltar during CANIGO. Deep-Sea Res. II 49, 4051–4067.
Gascard, J.C., Richez, C., 1985. Water masses and circulation in the Western Alboran sea and in the Straits of Gibraltar. Prog. Oceanogr. 15, 157–216. https://doi.org/10.1016/0079-6611(85)90031-X.
Gerkema, T., Zimmerman, J., 2008. An introduction to internal waves. Lecture Notes, Royal NIOZ, Texel, p. 207.
Goes, M., Christophersen, J., Dong, S., Goni, G., Baringer, M.O., Goes, M., Christophersen, J., Dong, S., Goni, G., Baringer, M.O., 2018. An Updated Estimate of Salinity for the Atlantic Ocean Sector Using Temperature-Salinity Relationships. J. Atmos. Oceanic Tech. 35, 1771–1784. https://doi.org/10.1175/JTECH-D-18-0029.1.
González, C.J., Álvarez, Ó., Mañanes, R., Izquierdo, A., Bruno, M., Gomiz, J.J., Chioua, J., López, L., 2013. Baroclinic M2 tidal circulation in Algeciras Bay and its implications for the water exchange with the Strait of Gibraltar: Observational and 3-D model results. J. Geophys. Res. Oceans 118, 5398–5411. https://doi.org/10.1002/jgrc.20404.
Hersbach, H., Bell, B., Berrisford, P., Biavati, G., Horányi, A., Muñoz Sabater, J., Nicolas, J., Peubey, C., Radu, R., Rozum, I., Schepers, D., Simmons, A., Soci, C., Dee, D., Thépaut, J-N., 2023. ERA5 hourly data on single levels from 1940 to present. Copernicus Climate Change Service (C3S) Climate Data Store (CDS), DOI: 10.24381/cds.adbb2d47.
Izquierdo, A., Tejedor, L., Sein, D.V., Backhaus, J.O., Brandt, P., Rubino, A., Kagan, B.A., 2001. Control Variability and Internal Bore Evolution in the Strait of Gibraltar: A 2-D Two-Layer Model Study. Estuarine, Coastal and Shelf Science 53, 637–651. https://doi.org/DOI: 10.1006/ecss.2000.0706.
La Violette, P.E., Arnone, R.A., 1988. A tide-generated internal waveform in the western approaches to the Strait of Gibraltar. J. Geophys. Res. Oceans 93, 15653–15790. https://doi.org/10.1029/JC093iC12p15653.
Lamb, K.G., 2003. Shoaling solitary internal waves: on a criterion for the formation of waves with trapped cores. J. Fluid Mech. 478, 81–100. https://doi.org/10.1017/S0022112002003269.
Lamb, K.G., 2014. Internal Wave Breaking and Dissipation Mechanisms on the Continental Slope/Shelf. Annu. Rev. Fluid Mech. 46, 231–254. https://doi.org/10.1146/annurev-fluid-011212-140701.
Lee, C.-Y., Beardsley, R.C., 1974. The Generation of Long Nonlinear Internal Waves in a Weakly Stratified Shear Flow. J. Geophys. Res. 79.
Liu, A.K., 1988. Analysis of Nonlinear Internal Waves in the New York Bight. J. Geophys. Res. 93, 12317. https://doi.org/10.1029/jc093ic10p12317.
Lorente, P., Piedracoba, S., Sotillo, M., Álvarez-Fanjul, E., 2019. Long-Term Monitoring of the Atlantic Jet through the Strait of Gibraltar with HF Radar Observations. J. Mar. Sci. Eng. 7, 3. https://doi.org/10.3390/jmse7010003.
Macías, D., García, C.M., Echevarría, F., Vázquez, A., Bruno, M., 2006. Tidal induced variability of mixing processes on Camarinal Sill (Strait of Gibraltar): A pulsating event. J. Mar. Syst. 60, 177–192. https://doi.org/10.1016/j.jmarsys.2005.12.003.
Macías, D., Martin, A.P., García-Lafuente, J., García, C.M., Yool, A., Bruno, M., Vázquez-Escobar, A., Izquierdo, A., Sein, D.V., Echevarría, F., 2007. Analysis of mixing and biogeochemical effects induced by tides on the Atlantic-Mediterranean flow in the Strait of Gibraltar through a physical-biological coupled model. Prog. Oceanogr. 74, 252–272. https://doi.org/10.1016/j.pocean.2007.04.006.
Macías, D., Lubián, L.M., Echevarría, F., Huertas, I.E., García, C.M., 2008. Chlorophyll maxima and water mass interfaces: Tidally induced dynamics in the Strait of Gibraltar. Deep-Sea Research I 55, 832–846. https://doi.org/10.1016/j.dsr.2008.03.008.
Macías, D., García-Gorriz, E., Stips, A., 2016. The seasonal cycle of the Atlantic Jet dynamics in the Alboran Sea: direct atmospheric forcing versus Mediterranean thermohaline circulation. Ocean Dyn. 66, 137–151. https://doi.org/10.1007/s10236-015-0914-y.
MEDAR Group, 2002. Medatlas 2002: Mediterranean and Black Sea Database of Temperature, Salinity and Bio-chemical Parameters Climatological Atlas. IFREMER 4 CDroms.
Millot, C., 2009. Another description of the Mediterranean Sea outflow. Prog. Oceanogr. 82, 101–124. https://doi.org/10.1016/j.pocean.2009.04.016.
Miramontes, E., Jouet, G., Thereau, E., Bruno, M., Penven, P., Guerin, C., Le Roy, P., Droz, L., Jorry, S.J., Hernández-Molina, F.J., Thiéblemont, A., Silva Jacinto, R., Cattaneo, A., 2020. The impact of internal waves on upper continental slopes: insights from the Mozambican margin (southwest Indian Ocean). Earth Surface Processes and Landforms esp.4818. https://doi.org/10.1002/esp.4818.
Morozov, E.G., Trulsen, K., Velarde, M.G., Vlasenko, V.I., 2002. Internal Tides in the Strait of Gibraltar. J. Phys. Oceanogr. 32, 3193–3206. https://doi.org/10.1175/1520-0485(2002)032<3193:ITITSO>2.0.CO;2.
Navarro, G., Vicent, J., Caballero, I., Gómez-Enri, J., Morris, E.P., Sabater, N., Macías, D., Bolado-Penagos, M., Gomiz, J.J., Bruno, M., Caldeira, R., Vázquez, Á., 2018. Improving the analysis of biogeochemical patterns associated with internal waves in the strait of Gibraltar using remote sensing images. Estuar. Coast. Shelf Sci. 204, 1–13. https://doi.org/10.1016/j.ecss.2018.02.009.
Oguz, T., Mourre, B., Tintoré, J., 2017. Modulation of frontogenetic plankton production along a meandering jet by zonal wind forcing: An application to the Alboran Sea. J. Geophys. Res. Oceans. https://doi.org/10.1002/2017JC012866.
Pistek, P., La Violette, P.E., 1999. Observations of the suppression of tide-generated nonlinear internal wave packets in the Strait of Gibraltar. J. Mar. Syst. 20, 113–128. https://doi.org/10.1016/S0924-7963(98)00073-6.
Puig, P., Palanques, A., Guillén, J., El Khatab, M., 2004. Role of internal waves in the generation of nepheloid layers on the northwestern Alboran slope: Implications for continental margin shaping. J. Geophys. Res. C: Oceans 109, 1–11. https://doi.org/10.1029/2004JC002394.
Ramírez-Romero, E., Macías, D., Bruno, M., Reyes, E., Navarro, G., García, C.M., 2012. Submesoscale, tidally-induced biogeochemical patterns in the Strait of Gibraltar. Estuar. Coast. Shelf Sci. 101, 24–32. https://doi.org/10.1016/j.ecss.2012.02.010.
Ramírez-Romero, E., Macías, D., García, C.M., Bruno, M., 2014. Biogeochemical patterns in the Atlantic Inflow through the Strait of Gibraltar. Deep Sea Res. Part 1 Oceanogr. Res. Pap. 85, 88–100. https://doi.org/10.1016/j.dsr.2013.12.004.
Reseghetti, F., 2007. Empirical reconstruction of salinity from temperature profiles with phenomenological constraints. Ocean Sci. Discuss. 4, 1–39.
Sala, I., Bolado-Penagos, M., Bartual, A., Bruno, M., García, C.M., López-Urrutia, Á., González-García, C., Echevarría, F., 2022. A Lagrangian approach to the Atlantic Jet entering the Mediterranean Sea: Physical and biogeochemical characterization. J. Mar. Syst. 226, 103652 https://doi.org/10.1016/j.jmarsys.2021.103652.
Sánchez-Garrido, J.C., García-Lafuente, J., Criado-Aldeanueva, F., Baquerizo, A., Sannino, G., 2008. Time-spatial variability observed in velocity of propagation of the internal bore in the Strait of Gibraltar. J. Geophys. Res. Oceans 113, 1–6. https://doi.org/10.1029/2007JC004624.
Sánchez-Garrido, J.C., Naranjo, C., Macías, D., García-Lafuente, J., Oguz, T., 2015. Modeling the impact of tidal flows on the biological productivity of the Alboran Sea. J. Geophys. Res. Oceans 120, 7329–7345. https://doi.org/10.1002/2015JC010885.
Sánchez-Román, A., Sannino, G., García-Lafuente, J., Carillo, A., Criado-Aldeanueva, F., 2009. Transport estimates at the western section of the Strait of Gibraltar: A combined experimental and numerical modeling study. J. Geophys. Res. Oceans 114, 1–15. https://doi.org/10.1029/2008JC005023.
Sannino, G., Bargagli, A., Artale, V., 2004. Numerical modeling of the semidiurnal tidal exchange through the Strait of Gibraltar. J. Geophys. Res. C: Oceans 109, 1–23. https://doi.org/10.1029/2003JC002057.
Sarhan, T., García-Lafuente, J., Vargas, M., Vargas, J.M., Plaza, F., 2000. Upwelling mechanisms in the northwestern Alboran Sea. J. Mar. Syst. 23, 317–331. https://doi.org/10.1016/S0924-7963(99)00068-8.
Soto-Navarro, J., Lorente, P., Álvarez-Fanjul, E., Sánchez-Garrido, J.C., García-Lafuente, J., 2016. Surface circulation at the Strait of Gibraltar: A combined HF radar and high resolution model study. J. Geophys. Res. Oceans 121, 2016–2034. https://doi.org/10.1002/2016JC012335.
Tsimplis, M.N., Bryden, H.L., 2000. Estimation of the transports through the Strait of Gibraltar. Deep Sea Res., Part I 47, 2219–2242.
Vázquez, A., Stashchuk, N., Vlasenko, V., Bruno, M., Izquierdo, A., Gallacher, P.C., 2006. Evidence of multimodal structure of the baroclinic tide in the Strait of Gibraltar. Geophys. Res. Lett. 33 https://doi.org/10.1029/2006GL026806.
Vázquez, A., Bruno, M., Izquierdo, A., Macías, D., Ruiz-Cañavate, A., 2008. Meteorologically forced subinertial flows and internal wave generation at the main sill of the Strait of Gibraltar. Deep Sea Res. Part 1 Oceanogr. Res. Pap. 55, 1277–1283. https://doi.org/10.1016/j.dsr.2008.05.008.
Vázquez, A., Flecha, S., Bruno, M., Macías, D., Navarro, G., 2009. Internal waves and short-scale distribution patterns of chlorophyll in the Strait of Gibraltar and Alborán Sea. Geophys. Res. Lett. 36 https://doi.org/10.1029/2009GL040959.
Villamaña, M., Mouriño-Carballido, B., Marañón, E., Cermeño, P., Chouciño, P., da Silva, J.C.B., Díaz, P.A., Fernández-Castro, B., Gilcoto, M., Graña, R., Latasa, M., Magalhaes, J.M., Luis Otero-Ferrer, J., Reguera, B., Scharek, R., 2017. Role of internal waves on mixing, nutrient supply, and phytoplankton community structure during spring and neap tides in the upwelling ecosystem of Ría de Vigo (NW Iberian Peninsula). Limnol. Oceanogr. 62, 1014–1030. https://doi.org/10.1002/lno.10482.
Vlasenko, V., Stashchuk, N., Hutter, K., 2005. Baroclinic Tides. Cambridge University Press, New York.
Vlasenko, V., Sanchez Garrido, J.C., Stashchuk, N., Garcia Lafuente, J., Losada, M., 2009. Three-Dimensional Evolution of Large-Amplitude Internal Waves in the Strait of Gibraltar. J. Phys. Oceanogr. 39, 2230–2246. https://doi.org/10.1175/2009JPO4007.1.
Watson, G., Robinson, I.S., 1990. A study of internal wave propagation in the Strait of Gibraltar using shore-based marine radar images. Journal of Physical Oceanography 20, 374–394. https://doi.org/doi:10.1175/1520-0485(1990)020<0374:ASOIWP>2.0.CO;2.
Wesson, J.C., Gregg, M.C., 1994. Mixing at Camarinal Sillin the Strait of Gibraltar. J. Geophys. Res. 99, 9847–9878.